AIAA JOURNAL
Vol. 49, No. 1, January 2011

# Multibody Dynamic Approach of Flight Dynamics and Nonlinear Aeroelasticity of Flexible Aircraft

Zhenjun Zhao* and Gexue Ren†
*Tsinghua University, 100084 Beijing, People's Republic of China*

DOI: 10.2514/1.45334

**The flight and structural dynamics of a very flexible aircraft, especially while maneuvering, are more tied together than those of conventional aircraft. Hence, it is necessary to study the coupled effects of flight dynamics, aeroelasticity, and control. This paper presents a multibody dynamic approach in which the flexible aircraft is modeled as a feedback-controlled multibody system under aerodynamic forces. The governing equations of the system are established by combining the equations of a multibody system, the ONERA aerodynamic model, and that of controls. The trim state of the flexible aircraft is solved using a dynamic relaxation method around which the perturbation equation is derived and solved for system stability. To demonstrate the advantage of multibody dynamics in modeling the constrained system undergoing large displacements and rotations, the proposed approach is applied to the flexible aircraft in level flight and in the circling and dive–loop–climb maneuvers. Beyond the flutter boundary, the limit cycle oscillations response is solved, in which several interesting aspects of flexible aircraft flutter are revealed. In the end, the joint flutter and attitude control is used to suppress flutter response and stabilize attitude.**



## Nomenclature

| | | |
|---|---|---|
| $\boldsymbol{A}$, $\boldsymbol{B}$, $\boldsymbol{C}$, $\boldsymbol{D}$ | = | system matrix, control matrix, observe matrix, and transfer matrix |
| $a$ | = | acceleration, m/s$^2$ |
| $b$, $c$, $\Delta l$ | = | airfoil semichord length, airfoil chord length, and wing segment span length, m |
| $C$ | = | aerodynamic coefficient |
| $\boldsymbol{C}_s$, $\boldsymbol{G}_s$, $\boldsymbol{K}_s$ | = | damping matrix, gyroscope matrix, and stiffness matrix |
| $d$ | = | coefficients of backward differentiation formulas |
| $F$, $\boldsymbol{F}$ | = | force, force vector, N |
| $\boldsymbol{f}$, $\boldsymbol{g}$ | = | differential equation, algebraic equation |
| $\boldsymbol{G}$ | = | mapping matrix |
| $\boldsymbol{H}$ | = | transfer function of feedback control |
| $h$ | = | deflection, m |
| $\boldsymbol{I}$, $\boldsymbol{J}$ | = | inertia matrix, inertia matrix corresponding to Euler parameter |
| $I$ | = | cross sectional inertia moment, m$^4$ |
| $k$ | = | coefficient of control law |
| $\boldsymbol{m}$, $\boldsymbol{M}$ | = | mass matrix, generalized mass matrix, kg |
| $n$ | = | total number |
| $\boldsymbol{O}$ | = | coefficient matrix of the ONERA airfoil equation |
| $\boldsymbol{P}$ | = | generalized force |
| $p$, $q$, $r$ | = | parameters of the ONERA airfoil equation |
| $\boldsymbol{Q}$ | = | generalized force corresponding to Coriolis force and centrifugal force |
| $\boldsymbol{q}$, $\boldsymbol{v}$ | = | generalized coordinate vector, generalized velocity vector |
| $\boldsymbol{s}$ | = | local vector under the body-fixed reference frame |
| $S$ | = | area of control surface or wing, m$^2$ |
| $s$ | = | integrator order |
| $\boldsymbol{T}$ | = | generalized forces corresponding to the Euler parameter |
| $T$, $U$ | = | kinetic energy of the system, potential energy of the system, J |
| $t$, $t_\tau$ | = | time, dimensionless time, s |
| $\boldsymbol{u}$, $\boldsymbol{x}$, $\boldsymbol{y}$ | = | control vector, state vector and observed variable of control system |
| $V$, $\boldsymbol{V}$ | = | speed, velocity, m/s |
| $x$, $y$, $z$, $\boldsymbol{r}$ | = | Cartesian coordinates, and Cartesian coordinate vector, m |
| $\boldsymbol{z}$ | = | integral variables |
| $\alpha$ | = | torsion angle, rad |
| $a_{oz}$ | = | slope of linear static aerodynamic coefficient curve, 1/rad |
| $\delta$, $\boldsymbol{\delta}$ | = | deflection of control surface, deflection vector of control surface, rad |
| $\boldsymbol{\zeta}$, $\boldsymbol{\mu}$ | = | variable, input vector of the ONERA airfoil equation |
| $\eta$ | = | efficiency coefficient of the control surface |
| $\theta$, $\psi$, $\phi$ | = | pitch angle, yaw angle, and roll angle, rad |
| $\lambda$, $\boldsymbol{\lambda}$ | = | Euler parameter, Euler parameter vector |
| $\rho$ | = | density, kg/m$^3$ |
| $\sigma$, $\boldsymbol{\sigma}$ | = | Lagrange multiplier, Lagrange multiplier vector |
| $\Phi$, $\boldsymbol{\Phi}$ | = | constraint equation, constraint equation vector |
| $\chi$ | = | sweepback angle, rad |

*Subscripts*

| | | |
|---|---|---|
| $b$, $c$, $s$ | = | body, constraint, and accelerometer |
| $L$, $D$, $M$ | = | lift, drag, and pitching moment |
| LA, RA, LF, RF | = | left aileron, right aileron, left flap, and right flap |
| $p$, $d$ | = | proportional, derivative (control) |
| $R$, LE, RE | = | rudder, left elevator, and right elevator |
| $z$, $za$, $zb$ | = | aerodynamic (coefficient), linear aerodynamic (coefficient), and nonlinear aerodynamic (coefficient) |
| 1/4 | = | wing quarter-chord |
| $\cdot$ | = | partial derivative |
| $\tilde{}$ | = | skew-symmetric matrix |
| $\bar{}$ | = | trim state (variable), or reference (variable) of control system |
| $\hat{}$ | = | perturbation (variable around the trim state) |
| $\overset{\frown}{}$ | = | (polynomial) at previous time steps |

*Superscripts*

| | | |
|---|---|---|
| ac | = | aerodynamic center |
| $c$ | = | control surface |
| $e$ | = | effective |
| $F$, $A$ | = | flutter control, attitude control |

Received 7 May 2009; accepted for publication 31 May 2010. 

*Ph.D. Candidate, School of Aerospace; zhaozhenjunzzj@163.com.
†Professor, School of Aerospace; rengx@mail.tsinghua.edu.cn.

| | | |
|---|---|---|
| $g, p, b, a$ | = | gravity, propulsion force, elastic force of beam, and aerodynamic force |
| hf, pf, fw | = | heading of fuselage, plunge of fuselage, and flap of wing |
| $I$ | = | instantaneous |
| $i, d$ | = | independent, dependent (variable) |
| $L, D, M$ | = | lift force, drag force, and pitching moment ($L = 0$ denotes zero lift) |
| lw | = | local wind (velocity) |
| $t$ | = | total |
| $\infty$ | = | freestream (velocity) |

## I. Introduction

THIS research is motivated by the necessity to study the coupled effects of flight dynamics, aeroelasticity, and control of very flexible aircraft, such as high-altitude long-endurance (HALE) aircraft with high-aspect-ratio wings, which may undergo large deflections in maneuvering [1,2], and the lower frequency elastic modes of which may also susceptible to the excitation of flight controls [3].

Aeroelasticity is a long-standing but challenging topic in aircraft designing. Linear aeroelasticity has already been well understood since the 1950s [4–6], while nonlinear aeroelasticity has also been studied for nearly two decades, as reviewed by Dowell et al. [7,8]. Considerable research has been carried out to study the effect of nonlinearity on aeroelastic behavior. In these studies, nonlinearity included structural nonlinearity, stall nonlinearity, and free-play nonlinearity of the control surface. Limit cycle oscillations (LCOs) have also been found in nonlinear aeroelasticity [9,10].

With the development of the very flexible aircraft, the interaction between flight dynamics and aeroelasticity has come to attract the attention of several researchers. Patil and Hodges [11] as well as Chang et al. [12] studied the flight dynamics of a flexible flying wing and aircraft considering nonlinear structural deformation. Shearer and Cesnik [13] focused on the characterization of the response of the very flexible aircraft in flight. Meirovitch and Tuzcu [14] presented a unified theory for flight dynamics, aeroelasticity, and control, in which the rigid-body motions of the fuselage and elastic displacements of flexible components relative to the fuselage have been considered. Nguyen [3] presented an integrated flight dynamic modeling method for the flexible aircraft by incorporating aeroelasticity effects. In these studies, the finite element method and modal reduction technique have been used as the basic modeling methodologies.

The constrained system containing rigid and flexible components can be conveniently modeled using the multibody dynamic approach, which is based on the differential-algebraic equation (DAE) [15–17]. In recent years, the multibody dynamic approach has already been applied to fluid–structure coupling analysis [18] and multiphysics coupling analysis [19]. This approach has also elicited attention from the aeroelastic community. Bauchau et al. [20] modeled rotorcraft systems using a multibody dynamic approach. Das et al. [21,22] used the plate and shell elements of multibody dynamics to model helicopter blades. Scarlett et al. [23] simulated the aeroelastic response of the folding wing of an unmanned combat aerial vehicle using their integrated aeroelastic simulation tool.

This paper aims to present an integrated approach of flight dynamics, nonlinear aeroelasticity, and control based on multibody dynamics. The aircraft, consisting of a fuselage, wing structures, and control surface mechanisms, was taken as a multibody system. Aerodynamic force was determined using the ONERA aerodynamic model, and feedback control was embedded for attitude and flutter controls of the fuselage and wings, respectively. Trim condition was obtained by dynamic relaxation under attitude and throttle controls. Then the perturbation equation of the multibody system was derived around the trim state. Several numerical examples of wing models and flexible aircraft are provided in this paper. In the numerical examples, the presented approach was applied to the trimming and stability analyses of the wing model, through which the flutter critical velocity and system instability mode were identified. Beyond the flutter boundary, the LCO response was solved. The trim condition of the flexible aircraft was then obtained using dynamic relaxation under attitude and throttle controls. The coupled dynamic behaviors of the flutter and flight of the flexible aircraft in level flight were studied. The same dynamic behaviors were also studied during the circling and dive–loop–climb maneuvers. The flutter and attitude joint control was used to suppress limit cycle response and stabilize aircraft attitude.

## II. Multibody Dynamic Modeling of the Flexible Aircraft

The flexible aircraft is a typical multibody system consisting of a fuselage, wing structures, and control surface mechanisms (Fig. 1). It can be conveniently modeled with multibody dynamics. The aircraft is taken as a multibody system consisting of rigid bodies connected by constraints and finite segment beams. The fuselage, fin, rudder, and tails are modeled as interconnected rigid bodies with constraints. The wings, flaps, and ailerons are modeled as the segments connected with flexible beams.

In the multibody dynamic approach, the position and attitude of every rigid body can be described by Cartesian coordinate $r$ of its mass center and Euler parameter $\lambda$, which are both taken as the generalized coordinates of the rigid body as

$$\boldsymbol{q} = [\boldsymbol{r}^T \quad \boldsymbol{\lambda}^T]^T \tag{1}$$

where

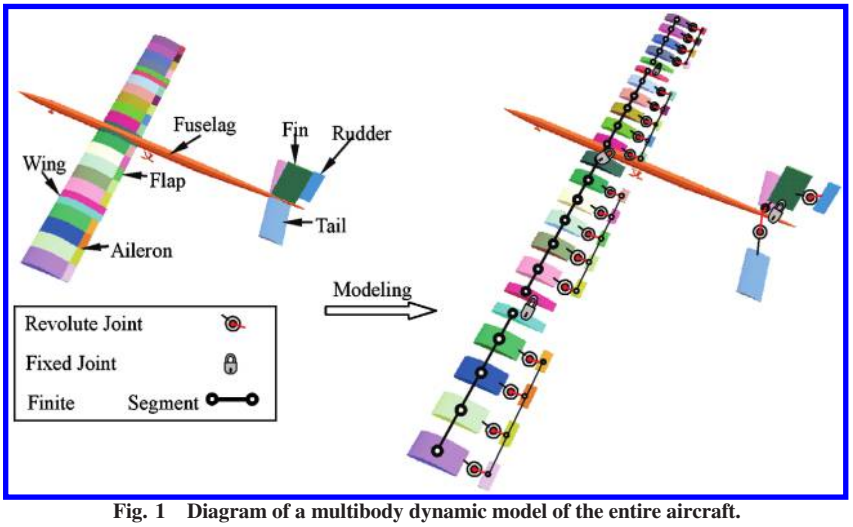


**Fig. 1 Diagram of a multibody dynamic model of the entire aircraft.**

$$\boldsymbol{r} = [x, y, z]^T \qquad \boldsymbol{\lambda} = [\lambda^0, \lambda^1, \lambda^2, \lambda^3]^T \tag{2}$$

According to Euler's finite displacement theorem, the orientation of any rigid body can be achieved by a single rotation about an axis, based on the Euler parameters [24] defined as

$$\lambda^0 = \cos(\theta/2) \qquad \lambda^1 = n^x \sin(\theta/2) \qquad \lambda^2 = n^y \sin(\theta/2)$$
$$\lambda^3 = n^z \sin(\theta/2) \tag{3}$$

where $n^x$, $n^y$, and $n^z$ are the three components of the orientation axis, and $\theta$ is the angle of rotation.

The four Euler parameters are dependent on one another, satisfying the following normalization constraint:

$$\Phi^{\lambda} = \boldsymbol{\lambda}^T \boldsymbol{\lambda} - 1 = 0 \tag{4}$$

All aircraft parts are represented in a coupled system by constraint equations [16]. The middle wing segment and fin are fixed to the fuselage, the tail is joined to the fuselage by a revolute joint, and the rudder is joined to the fin by a revolute joint. Every flap segment or aileron segment is joined to a corresponding wing segment by a revolute joint. The angle of the revolute joint is controlled by the angular displacement or angular velocity constraint. All constraints, including the Euler parameter normalization constraints, can be expressed in the following unified form:

$$\Phi_k(\boldsymbol{q}_1, \boldsymbol{q}_2, \ldots, \boldsymbol{q}_{n_b}, t) = 0 \qquad k = 1, \ldots, n_c \tag{5}$$

Using Lagrange's equations of the first kind [25], the dynamic equations of the system can be written as

$$\boldsymbol{M}_i \ddot{\boldsymbol{q}}_i - \boldsymbol{Q}_i - \boldsymbol{P}_i + \sum_{k=1}^{n_c} \Phi_{k,\boldsymbol{q}_i}^T \sigma_k = 0 \qquad i = 1, \ldots, n_b \tag{6}$$

where

$$\boldsymbol{M}_i = \begin{bmatrix} \boldsymbol{m}_i & 0 \\ 0 & \boldsymbol{J}_i \end{bmatrix}, \qquad \boldsymbol{J}_i = 4\boldsymbol{G}_i^T \boldsymbol{I}_i \boldsymbol{G}_i$$
$$\boldsymbol{G}_i = \begin{bmatrix} -\lambda_i^1 & \lambda_i^0 & \lambda_i^3 & -\lambda_i^2 \\ -\lambda_i^2 & -\lambda_i^3 & \lambda_i^0 & \lambda_i^1 \\ -\lambda_i^3 & \lambda_i^2 & -\lambda_i^1 & \lambda_i^0 \end{bmatrix} \qquad \boldsymbol{Q}_i = -\dot{\boldsymbol{M}}_i \dot{\boldsymbol{q}}_i + T_{i,\boldsymbol{q}_i}^T$$
$$T_i = \frac{1}{2} \dot{\boldsymbol{q}}_i^T \boldsymbol{M}_i \dot{\boldsymbol{q}}_i, \qquad T_{i,\boldsymbol{q}_i} = [T_{i,\boldsymbol{r}_i} \quad T_{i,\boldsymbol{\lambda}_i}] \qquad \boldsymbol{P}_i = [\boldsymbol{F}_i^T \quad \boldsymbol{T}_i^T]^T$$
$$\Phi_{k,\boldsymbol{q}_i} = [\Phi_{k,\boldsymbol{r}_i} \quad \Phi_{k,\boldsymbol{\lambda}_i}] \tag{7}$$

The dynamic equations of each body are coupled by the Lagrange multiplier $\sigma_k$ and the Jacobian matrix $\Phi_{k,\boldsymbol{q}_i}$ of constraint Eq. (5). The generalized force $\boldsymbol{P}_i$ contains four parts (gravity, propulsion force, aerodynamic force, and the elastic beam force), and these are expressed as

$$\boldsymbol{P}_i = \boldsymbol{P}_i^g + \boldsymbol{P}_i^p + \boldsymbol{P}_i^b + \boldsymbol{P}_i^a \tag{8}$$

### A. Generalized Force of Gravity

The gravity $\boldsymbol{F}_i^g$ is a concentrated force acting on the mass center of the rigid body. Using the principle of virtual work, $\boldsymbol{P}_i^g$ is expressed in the following simple form:

$$\boldsymbol{P}_i^g = \begin{bmatrix} \boldsymbol{F}_i^g \\ \boldsymbol{0}_{4\times 1} \end{bmatrix} \tag{9}$$

### B. Generalized Propulsion Force

The propulsion force $\boldsymbol{F}_i^p$ is a concentrated force acting on the fuselage. Using the principle of virtual work, $\boldsymbol{P}_i^p$ is derived as

$$\boldsymbol{P}_i^p = \begin{bmatrix} \boldsymbol{F}_i^p \\ \boldsymbol{T}_i^p \end{bmatrix} \tag{10}$$

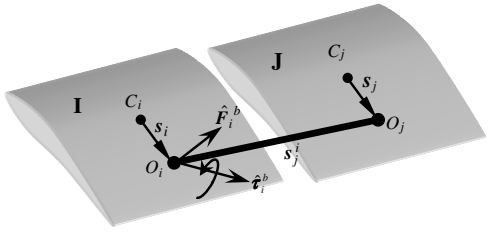


**Fig. 2 Representation of the finite segment beam.**

where

$$\boldsymbol{T}_i^p = 2\boldsymbol{G}_i^T \boldsymbol{\tau}_i^p, \qquad \boldsymbol{\tau}_i^p = \tilde{\boldsymbol{s}}_i^p \boldsymbol{F}_i^p \tag{11}$$

The vector of the action point of the propulsion force under the body-fixed reference frame of the fuselage is $\boldsymbol{s}_i^p$. Meanwhile, $\boldsymbol{T}_i^p$ is the generalized force corresponding to the Euler parameter, where $\boldsymbol{\tau}_i^p$ is the moment under the body-fixed reference frame, and $2\boldsymbol{G}_i^T$ is the mapping matrix from $\boldsymbol{\tau}_i^p$ to $\boldsymbol{T}_i^p$.

### C. Generalized Force Contributed by the Elastic Force of Finite Segment Beam

Using the finite segment approach, the flexible wing is assumed to consist of a set of rigid segments that are connected by massless beam segments [26]. As shown in Fig. 2, $O_i$ and $O_j$ are the nodes of two beam segments, and $C_i$ and $C_j$ are the mass centers of the rigid segments.

According to the assumption of small relative deformation, every beam segment is equivalent to a generalized linear spring element, and its stiffness matrix can be derived from the finite element beam theory [27]. In this sense, $\hat{\boldsymbol{F}}_i^b$ and $\hat{\boldsymbol{\tau}}_i^b$ can be regarded as a generalized linear spring force and moment acting on body I (Fig. 2).

Using the principle of virtual work, the generalized forces contributed by the elastic force of the finite segment beam are derived as

$$\boldsymbol{P}_b^i = \begin{bmatrix} \boldsymbol{F}_i^b \\ \boldsymbol{T}_i^b \end{bmatrix}, \qquad \boldsymbol{P}_b^j = \begin{bmatrix} \boldsymbol{F}_j^b \\ \boldsymbol{T}_j^b \end{bmatrix} \tag{12}$$

where

$$\boldsymbol{T}_i^b = 2\boldsymbol{G}_i^T \boldsymbol{\tau}_i^b, \qquad \boldsymbol{F}_j^b = -\boldsymbol{F}_i^b, \qquad \boldsymbol{T}_j^b = 2\boldsymbol{G}_j^T \boldsymbol{\tau}_j^b$$
$$\boldsymbol{\tau}_i^b = \hat{\boldsymbol{\tau}}_i^b + \tilde{\boldsymbol{s}}_i \hat{\boldsymbol{F}}_i^b, \qquad \boldsymbol{\tau}_j^b = -(\hat{\boldsymbol{\tau}}_i^b + \tilde{\boldsymbol{s}}_j \hat{\boldsymbol{F}}_i^b + \tilde{\boldsymbol{s}}_j^i \hat{\boldsymbol{F}}_i^b) \tag{13}$$

The vectors from $C_i$ to $O_i$, $C_j$ to $O_j$, and $O_j$ to $O_i$ are $\boldsymbol{s}_i$, $\boldsymbol{s}_j$, and $\boldsymbol{s}_j^i$, respectively. In addition, $\boldsymbol{T}_i^b$ and $\boldsymbol{T}_j^b$ are the generalized forces corresponding to the Euler parameter acting on bodies $I$ and $J$, respectively, where $\boldsymbol{\tau}_i^b$ is the moment acting on body $I$ and $\boldsymbol{\tau}_j^b$ is the moment acting on body $J$. Finally, $2\boldsymbol{G}_i^T$ and $2\boldsymbol{G}_j^T$ are the mapping matrixes from $\boldsymbol{\tau}_i^b$ to $\boldsymbol{T}_i^b$ and from $\boldsymbol{\tau}_j^b$ to $\boldsymbol{T}_j^b$, respectively.

### D. Generalized Aerodynamic Force

The aerodynamic forces are evaluated by combining the strip theory [28] and ONERA model [29], in which each airfoil strip corresponds to one wing segment in the structural model. The generalized aerodynamic force $\boldsymbol{P}_i^a$ will be developed in Sec. III.

## III. Aerodynamic Model

The lift, drag, and aerodynamic moment are expressed as

$$F_i^L = \tfrac{1}{2}\rho(V_i^{\infty})^2 (C_L)_i c \Delta l_i \qquad F_i^D = \tfrac{1}{2}\rho(V_i^{\infty})^2 (C_D)_i c \Delta l_i$$
$$\tau_i^M = \tfrac{1}{2}\rho(V_i^{\infty})^2 (C_M)_i c^2 \Delta l_i \tag{14}$$

The aerodynamic coefficients $C_L$, $C_M$, and $C_D$ of the airfoil are computed using the ONERA equation. The freestream velocity of the flight model varies with the motion of the wing, and is defined as the vector difference between the local wind velocity and the velocity of

the aerodynamic center of the wing projected in the airfoil plane depicted as [30]

$$\boldsymbol{V}_i^{\infty} = \boldsymbol{V}_i^{\mathrm{lw}} - \boldsymbol{V}_i^{\mathrm{ac}} \tag{15}$$

When $\boldsymbol{V}_i^{\mathrm{ac}} = 0$, the above mentioned model is reduced to the wind-tunnel model.

### A. ONERA Airfoil Equation

The ONERA airfoil equation [31] can be reformulated in the following matrix form:

$$\begin{cases} \dot{\boldsymbol{\zeta}}_z + \boldsymbol{O}_z \boldsymbol{\zeta}_z + \boldsymbol{\mu}_z = 0 \\ C_z = C_{za} + C_{zb} \end{cases} \qquad z = L, M, \text{ or } D \tag{16}$$

If $z = L$ or $M$, then we arrive at

$$\begin{gathered} \boldsymbol{\zeta}_z = [\, C_{z\gamma} \quad C_{zb} \quad \xi \,]^T \\ C_{za} = t_\tau p_{z1} \dot{\alpha}^e + t_\tau^2 p_{z2} \ddot{\alpha}^I + t_\tau p_{z3} \dot{\alpha}^I + C_{z\gamma} \\ \Delta C_z = a_{oz} \alpha^e - C_z, \qquad \boldsymbol{O}_z = \frac{1}{t_\tau} \begin{bmatrix} q_1 & 0 & 0 \\ 0 & 0 & -1 \\ 0 & r_{z2} & r_{z1} \end{bmatrix} \\ \xi = t_\tau \dot{C}_{zb} \\ \boldsymbol{\mu}_z = \frac{1}{t_\tau} \begin{bmatrix} -q_1 a_{oz} (\alpha^e + t_\tau \dot{\alpha}^I) - q_2 a_{oz} (t_\tau \dot{\alpha}^e + t_\tau^2 \ddot{\alpha}^I) \\ 0 \\ r_{z2} \Delta C_z + t_\tau r_{z3} \frac{\partial \Delta C_z}{\partial \alpha^I} \dot{\alpha}^e \end{bmatrix} \end{gathered} \tag{17}$$

If $z = D$, then we arrive at

$$\begin{gathered} \boldsymbol{\zeta}_z = [\, C_{Db} \quad \xi \,]^T \\ \Delta C_D = -0.042 \alpha^e - 0.1473 (\alpha^e)^2 - 4.923 (\alpha^e)^3 \\ C_{Da} = 0.014 \qquad \boldsymbol{O}_z = \frac{1}{t_\tau} \begin{bmatrix} 0 & -1 \\ r_{D2} & r_{D1} \end{bmatrix} \\ \boldsymbol{\mu}_z = \frac{1}{t_\tau} \begin{bmatrix} 0 \\ r_{D2} \Delta C_z + t_\tau r_{D3} \dot{\alpha}^e \end{bmatrix} \\ \xi = t_\tau \dot{C}_{zb}, t_\tau = b / V^{\infty} \end{gathered} \tag{18}$$

where

$$\begin{gathered} \alpha^e = \alpha^I - \frac{\dot{h}_{1/4}}{V^{\infty}} - \alpha^{L=0} + \alpha^c, \qquad \alpha^c = \delta \eta \\ \eta = \sqrt{(S^c / S^t) \cos \chi} \end{gathered} \tag{19}$$

The efficiency coefficient $\eta$ of the control surface is approximately evaluated according to the procedure described in [32]. All variables such as $\alpha^I$, $\dot{\alpha}^I$, $\ddot{\alpha}^I$, $h_{1/4}$, $\dot{h}_{1/4}$, and $\ddot{h}_{1/4}$ can be expressed in $\boldsymbol{q}$, $\dot{\boldsymbol{q}}$, and $\ddot{\boldsymbol{q}}$. The input vector $\boldsymbol{\mu}_z$ of the ONERA airfoil equation could be expressed in the following form:

$$\boldsymbol{\mu}_z = \boldsymbol{\mu}_z (\boldsymbol{q}, \dot{\boldsymbol{q}}, \ddot{\boldsymbol{q}}, \delta) \tag{20}$$

For simplicity, all parameters used in this study, including $p_{z1}$, $p_{z2}$, $p_{z3}$, $q_1$, $q_2$, $r_{z1}$, $r_{z2}$, $r_{z3}$, $r_{D1}$, $r_{D2}$, $r_{D3}$, $\Delta C_z$, and $\partial \Delta C_z / \partial \alpha^I$, were the same as those given in [31], which were only applicable to the NACA 0012 airfoil. In comparison, the proposed model can be easily adapted to other airfoils.

### B. Generalized Forces Contributed by Aerodynamic Force

The aerodynamic force and moment about the mass center are expressed as

$$\boldsymbol{F}_i^a = \boldsymbol{F}_i^L + \boldsymbol{F}_i^D \tag{21}$$

and

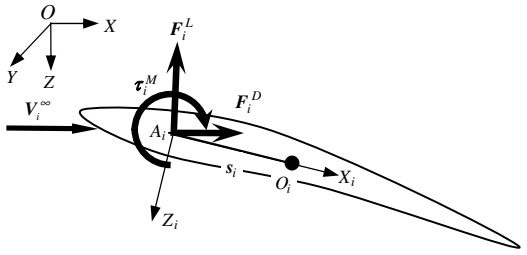


**Fig. 3 Aerodynamic force and aerodynamic moment of airfoil.**

$$\boldsymbol{\tau}_i^a = \tilde{\boldsymbol{s}}_i \boldsymbol{F}_i^L + \tilde{s}_i \boldsymbol{F}_i^D + \boldsymbol{\tau}_i^M \tag{22}$$

where $s_i$ is the vector of the quarter-chord tip in the mass center frame of the body (see Fig. 3).

Using the principle of virtual work, the generalized force corresponding to aerodynamic force is derived as

$$\boldsymbol{P}_i^a = \begin{bmatrix} \boldsymbol{F}_i^a \\ \boldsymbol{T}_i^a \end{bmatrix} \tag{23}$$

where

$$\boldsymbol{T}_i^a = 2 \boldsymbol{E}_i^T \boldsymbol{\tau}_i^a, \qquad \boldsymbol{E}_i = \begin{bmatrix} -\lambda_i^1 & \lambda_i^0 & -\lambda_i^3 & \lambda_i^2 \\ -\lambda_i^2 & \lambda_i^3 & \lambda_i^0 & -\lambda_i^1 \\ -\lambda_i^3 & -\lambda_i^2 & \lambda_i^1 & \lambda_i^0 \end{bmatrix} \tag{24}$$

The generalized force corresponding to the Euler parameter of the wing segment $I$ is $\boldsymbol{T}_i^a$, where $2\boldsymbol{E}_i^T$ is the mapping matrix from $\boldsymbol{\tau}_i^a$ to $\boldsymbol{T}_i^a$.

## IV. Feedback Control

The attitude, throttle, and flutter controls were embedded into the aircraft model to stabilize aircraft attitude and suppress limit cycle response. By observing $\psi$, $\theta$, $\phi$, $\dot{\psi}$, $\dot{\theta}$, $\dot{\phi}$, $a^f$, $a^w$, $v^h$, and $a^h$, the designed control law determined the control variables $\delta$ and $F^p$. The control surfaces were manipulated and the throttle was adjusted so that the aircraft maintained the given flight state and its wing flutter response was suppressed (see Fig. 4).

### A. Description of Control

The aim of attitude and throttle controls is to ensure that the aircraft achieves and maintains a given flight state. The flutter controller incorporating attitude control is used to suppress limit cycle response, in which the control surfaces and throttle are taken as actuators. The controlled, control, observed, and reference variables of the control system are listed in Table 1.

### B. Implementation of Control in Multibody Dynamics

Each control can be considered by transfer function $\boldsymbol{H}(s)$ of feedback control given as

$$\boldsymbol{u}(s) = \boldsymbol{H}(s) \boldsymbol{y}(s) \tag{25}$$

The state space realization of $\boldsymbol{H}(s)$ is obtained using the realization technique of controllable criterion in the control theory [33] and is written as $\sum(\boldsymbol{A}, \boldsymbol{B}, \boldsymbol{C}, \boldsymbol{D})$, by which the relationship between the control vector $\boldsymbol{u}$ and the observed variable $\boldsymbol{y}$ is expressed as

$$\begin{cases} \dot{\boldsymbol{x}} = \boldsymbol{A}\boldsymbol{x} + \boldsymbol{B}\boldsymbol{y} \\ \boldsymbol{u} = \boldsymbol{C}\boldsymbol{x} + \boldsymbol{D}\boldsymbol{y} \end{cases} \tag{26}$$

This system includes the three types of feedback controls, and the variables of Eq. (26) are defined as

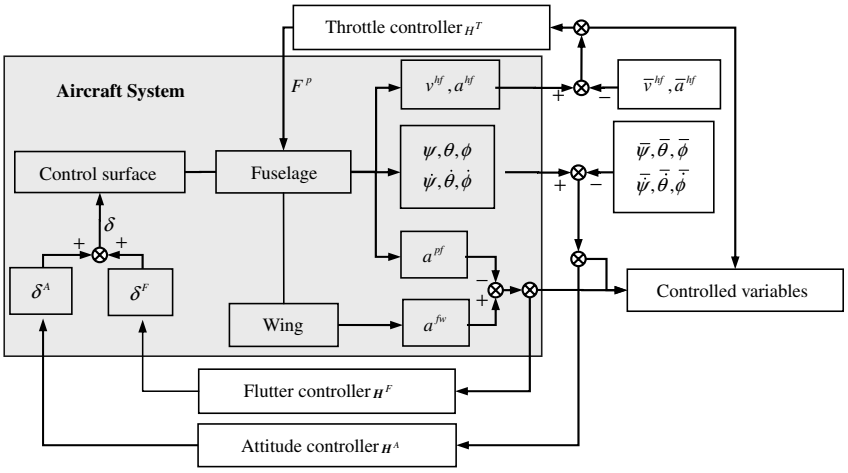


**Fig. 4 Control system diagram.**

$$\boldsymbol{y} = [\theta \quad \dot{\theta} \quad \psi \quad \dot{\psi} \quad \phi \quad \dot{\phi} \quad a^{\mathrm{pf}} \quad a_1^{\mathrm{fw}} \quad \cdots \quad a_{n_s}^{\mathrm{fw}} \quad v^{\mathrm{hf}} \quad a^{\mathrm{hf}}]^T$$

$$\boldsymbol{u} = [\delta^T \quad F^p]^T$$

$$\boldsymbol{\delta} = [\delta_R^A \quad \delta_{\mathrm{LE}}^A \quad \delta_{\mathrm{RE}}^A \quad \delta_{\mathrm{LA}}^A + \delta_{\mathrm{LA}}^F \quad \delta_{\mathrm{RA}}^A + \delta_{\mathrm{RA}}^F \quad \delta_{\mathrm{LF}}^F \quad \delta_{\mathrm{RF}}^F]^T \tag{27}$$

The observed variable $\boldsymbol{y}$ can be expressed as a function of the generalized coordinate $\boldsymbol{q}$, generalized velocity $\dot{\boldsymbol{q}}$, and generalized acceleration $\ddot{\boldsymbol{q}}$ as

$$\boldsymbol{y} = \boldsymbol{y}(\boldsymbol{q}, \dot{\boldsymbol{q}}, \ddot{\boldsymbol{q}}, t) \tag{28}$$

The control of each control surface is introduced into multibody system by the angular displacement constraint or the angular velocity constraint. The throttle control is implemented by the generalized force $\boldsymbol{P}^a$.

## V. Governing Equation of the Aircraft

Combining the multibody dynamic equation (6), the ONERA equation (16), and the state equation (26) of feedback control, the governing equation of the entire aircraft is obtained as

$$\begin{cases} \boldsymbol{M}\ddot{\boldsymbol{q}} - \boldsymbol{Q} - \boldsymbol{P} + \boldsymbol{\Phi}_q^T \boldsymbol{\sigma} = 0 \\ \dot{\boldsymbol{\zeta}}_z + \boldsymbol{O}_z \boldsymbol{\zeta}_z + \boldsymbol{\mu}_z = 0 \\ \boldsymbol{\Phi}(\boldsymbol{q}, \boldsymbol{u}, t) = 0 \\ \boldsymbol{y} = \boldsymbol{y}(\boldsymbol{q}, \dot{\boldsymbol{q}}, \ddot{\boldsymbol{q}}, t) \\ \dot{\boldsymbol{x}} = \boldsymbol{A}\boldsymbol{x} + \boldsymbol{B}\boldsymbol{y} \\ \boldsymbol{u} = \boldsymbol{C}\boldsymbol{x} + \boldsymbol{D}\boldsymbol{y} \end{cases} \tag{29}$$

Governing Eq. (29) can be solved through the time discretization and numerical integration scheme. This solution scheme is shown in Fig. 5 in which, for convenience, the superscripts $(n)$ and $(n+1)$ represent the governing variables at the$n$ and $n+1$ time steps, and the superscript $(m)$ represents the observed variables at the $m$ sampling step. Several variables are expressed in the form containing arguments for describing the implementation of control, and the generalized force $P$ is expressed in detailed form using Eq. (8).

**Table 1 Description of control**

| Controlled variable | Control variable | Observed variable | Reference variable |
|---|---|---|---|
| | *Attitude control* $\boldsymbol{H}^A$ | | |
| $\psi, \dot{\psi}$ | $\delta_R^A$ | $\psi, \dot{\psi}$ | $\bar{\psi}, \bar{\dot{\psi}}$ |
| $\theta, \dot{\theta}$ | $\delta_{\mathrm{LE}}^A, \delta_{\mathrm{RE}}^A$ | $\theta, \dot{\theta}$ | $\bar{\theta}, \bar{\dot{\theta}}$ |
| $\phi, \dot{\phi}$ | $\delta_{\mathrm{LA}}^A, \delta_{\mathrm{RA}}^A$ | $\phi, \dot{\phi}$ | $\bar{\phi}, \bar{\dot{\phi}}$ |
| | *Throttle control* $\boldsymbol{H}^T$ | | |
| $v^{\mathrm{hf}}$ | $F^p$ | $v^{\mathrm{hf}}, a^{\mathrm{hf}}$ | $\bar{v}^{\mathrm{hf}}, \bar{a}^{\mathrm{hf}}$ |
| | *Flutter control* $\boldsymbol{H}^F$ | | |
| $\lvert a_1^{\mathrm{fw}} - a^{\mathrm{pf}} \rvert \cdots$ | $\delta_{\mathrm{LA}}^F, \delta_{\mathrm{RA}}^F$ | $a_1^{\mathrm{fw}}, \ldots, a_{n_s}^{\mathrm{fw}}$ | $a^{\mathrm{pf}}$ |
| $\lvert a_{n_s}^{\mathrm{fw}} - a^{\mathrm{pf}} \rvert$ | $\delta_{\mathrm{LF}}^F, \delta_{\mathrm{RF}}^F$ | | |

The first three equations of Eq. (29) describe the aeroelastic system consisting of the multibody aircraft and aerodynamic models.

Denoting

$$\boldsymbol{z} = \begin{bmatrix} \boldsymbol{q} \\ \boldsymbol{v} \\ \boldsymbol{\zeta}_z \\ \boldsymbol{\varsigma} \end{bmatrix}, \qquad \boldsymbol{v} = \dot{\boldsymbol{q}}, \qquad \boldsymbol{f}(\boldsymbol{z}, \dot{\boldsymbol{z}}, t) = \begin{bmatrix} \dot{\boldsymbol{q}} - \boldsymbol{v} \\ \boldsymbol{M}\dot{\boldsymbol{v}} - \boldsymbol{Q} - \boldsymbol{P} \\ \dot{\boldsymbol{\zeta}}_z + \boldsymbol{O}_z \boldsymbol{\zeta}_z + \boldsymbol{\mu}_z \end{bmatrix}$$

$$\boldsymbol{\varsigma} = \begin{bmatrix} \boldsymbol{\sigma} \\ \boldsymbol{0} \\ \boldsymbol{0} \\ \boldsymbol{0} \end{bmatrix}, \qquad \boldsymbol{g}(\boldsymbol{z}, t) = \boldsymbol{\Phi}(\boldsymbol{q}, \boldsymbol{u}, t) \tag{30}$$

The first three equations of Eq. (29) can be expressed as

$$\begin{cases} \boldsymbol{f}(\boldsymbol{z}, \dot{\boldsymbol{z}}, t) + \boldsymbol{g}_z(\boldsymbol{z}, t)\boldsymbol{\varsigma} = 0 \\ \boldsymbol{g}(\boldsymbol{z}, t) = 0 \end{cases} \tag{31}$$

Equation (31) is a typical, fully implicit, and index-3 DAE, which can be integrated by numerical integration methods, such as the implicit Runge–Kutta method and backward differentiation formulas (BDFs) [34]. This work adopted the BDF method as the integration scheme. The underlying idea behind the use of BDF is to replace the differentiation of the integration variable by interpolating a

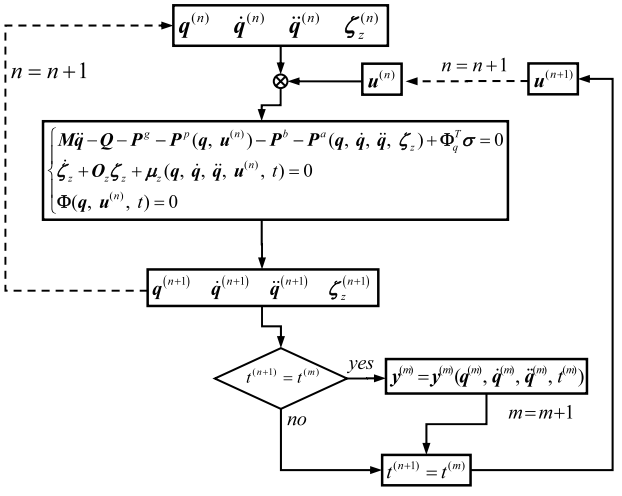


**Fig. 5 Solution scheme of the governing equation of the entire aircraft.**

polynomial through their values at current and previous time steps. It is written as

$$\dot{z}^{(n+1)} = \sum_{i=0}^{s} d_i \cdot z^{(n-s+1+i)} = d_s \cdot z^{(n+1)} + \hat{z}^{(n+1)} \tag{32}$$

where $s$ is the order of integrator, $d_i$ are the coefficients of BDF [34], and

$$\hat{z}^{(n+1)} = \sum_{i=0}^{s-1} d_i \cdot z^{(n-s+1+i)}$$

The starting procedure of the integrator is implemented by the BDF-1 scheme using an initial value and the initial step size. In the $n+1$ time step, all variables before this time step are known [$\hat{z}^{(n+1)}$ is the known variable at the $n+1$ time step, while $z^{(n+1)}$ is the unknown variable]. Substituting Eq. (32) into the first equation of Eq. (31), and satisfying Eq. (31) at the $n+1$ time step, we arrive at

$$\begin{aligned}\boldsymbol{\phi}(z^{(n+1)}) &= \begin{bmatrix} \boldsymbol{f}(z^{(n+1)}, d_s \cdot z^{(n+1)} + \hat{z}^{(n+1)}, t^{(n+1)}) + \boldsymbol{g}_z(z^{(n+1)}, t^{(n+1)})\boldsymbol{\varsigma} \\ \boldsymbol{g}(z^{(n+1)}, t^{(n+1)}) \end{bmatrix} \\ &= 0 \end{aligned} \tag{33}$$

The integration of Eq. (31) can come down to solving the nonlinear algebraic Eq. (33), which can, in turn, be solved by Newton iteration method.

Once the unknown variable $z^{(n+1)}$ is solved, other variables on the $n+1$ time step can be computed. Then there is a need to check if sampling must be done in order to update the observed variable $\boldsymbol{y}^{(s)}$ according to Eq. (28). By applying Eq. (32) to the state variable $x$, the discrete form of Eq. (26) is obtained as

$$\begin{cases} \boldsymbol{x}^{(n+1)} = \boldsymbol{A}_d^{-1}\boldsymbol{b}^{(n+1)} \\ \boldsymbol{u}^{(n+1)} = \boldsymbol{C}\boldsymbol{x}^{(n+1)} + \boldsymbol{D}\boldsymbol{y}^{(s)} \end{cases} \tag{34}$$

where

$$\begin{aligned} &\boldsymbol{A}_d = d_s\boldsymbol{I} - \boldsymbol{A}, \qquad \boldsymbol{b}^{(n)} = \boldsymbol{B}\boldsymbol{y}^{(s)} - \hat{\boldsymbol{x}}^{(n+1)}, \\ &\hat{\boldsymbol{x}}^{(n+1)} = \sum_{i=0}^{s-1} d_i \cdot \boldsymbol{x}^{(n-s+1+i)} \end{aligned} \tag{35}$$

Using Eq. (34), the control vector $\boldsymbol{u}^{(n+1)}$ could be determined and taken as the input variable of the next time step for control. The control surfaces are then adjusted according to the input variable under the action of the angular displacement constraint. This input variable brings the variation of input $\boldsymbol{\mu}_z$ of the ONERA dynamic equation due to $\alpha^c$. The variation of input $\boldsymbol{\mu}_z$ induces the change of aerodynamic force $\boldsymbol{P}^a$, which executes the flutter and attitude controls. The control variable $\boldsymbol{F}^p$ is thus adjusted to execute the throttle control.

## VI. Solution of Trim Condition by Dynamic Relaxation

In this work, trim condition was solved using dynamic relaxation of the controlled aircraft. The solution procedure can be described as follows: the objective state variables of trimming were taken as the control target of attitude and throttle controls, and the trim condition obtained by the trim equation of the rigid aircraft model were set as the initial parameter settings of the flexible aircraft model [35–37]. Then by integrating governing Eq. (29) in the time domain, the aircraft converges to steady flight state under the action of attitude and throttle controls, as well as damping. When the derivative items $\ddot{q}$ and $\dot{\eta}_z$ became less than the given error bound, the converged state variables

$$\bar{z} = [\,\bar{\boldsymbol{q}}^T \quad \dot{\bar{\boldsymbol{q}}}^T \quad \bar{\boldsymbol{\xi}}_z^T \quad \bar{\boldsymbol{\sigma}}^T\,]^T \tag{36}$$

and

$$\bar{\boldsymbol{u}} = [\,\bar{\boldsymbol{\delta}}^T \quad \bar{\boldsymbol{F}}^p\,]^T \tag{37}$$

satisfy the trim equation of the flexible aircraft approximately; that is,

$$\begin{cases} -\boldsymbol{Q}(\bar{\boldsymbol{q}}, \dot{\bar{\boldsymbol{q}}}, t) - \boldsymbol{P}(\bar{\boldsymbol{q}}, \dot{\bar{\boldsymbol{q}}}, \bar{\boldsymbol{u}}, \bar{\boldsymbol{\xi}}_z, t) + \boldsymbol{\Phi}_q^T(\bar{\boldsymbol{q}}, t)\boldsymbol{\sigma} = 0 \\ \boldsymbol{O}_z\bar{\boldsymbol{\xi}}_z + \boldsymbol{\mu}_z(\bar{\boldsymbol{q}}, \bar{\boldsymbol{u}}) = 0 \\ \boldsymbol{\Phi}(\bar{\boldsymbol{q}}, \bar{\boldsymbol{u}}, t) = 0 \end{cases} \tag{38}$$

In the dynamic relaxation simulation, the structural damping of the system could be increased artificially to accelerate the convergence of the trimming process. At the trim state, the aircraft maintained steady configuration, the deformation rate was zero, and the structural damping force item in trim Eq. (38) of the system was zero, so the high structural damping did not lead to the deviation of trim states.

In the frame of multibody system dynamics, the trim state can be conveniently solved very quickly with an implicit BDF of first order or second order. As shown in the presented examples, the trim state can usually be obtained in a few minutes. Of course, the trim state and condition can be also obtained by solving Eq. (38) directly.

## VII. Derivation of Perturbation Equation for Stability Analysis

The perturbation equation of the multibody system is derived around the trim state to study the stability of the system. The small perturbation $\tilde{z}$ around the trim state $\bar{z}$ is denoted as

$$\hat{z} = [\,\hat{\boldsymbol{q}}^T \quad \dot{\hat{\boldsymbol{q}}}^T \quad \hat{\boldsymbol{\xi}}_z^T \quad \hat{\boldsymbol{\sigma}}^T\,]^T \tag{39}$$

The integral variables $z$ can be expressed as

$$z = \bar{z} + \hat{z} \tag{40}$$

Substituting Eq. (40) into the first three equation of Eq. (29), the first-order linearization approximation around the trim state $\bar{z}$ is obtained as

$$\begin{cases} \bar{\boldsymbol{M}}\ddot{\hat{\boldsymbol{q}}} + (\bar{\boldsymbol{C}}_s + \bar{\boldsymbol{G}}_s)\dot{\hat{\boldsymbol{q}}} + \bar{\boldsymbol{K}}_s\hat{\boldsymbol{q}} + \boldsymbol{\Phi}_q^T\hat{\boldsymbol{\sigma}} = 0 \\ \dot{\hat{\boldsymbol{\xi}}}_z + \boldsymbol{O}_z\hat{\boldsymbol{\xi}}_z + (\boldsymbol{\mu}_z)_{\dot{\boldsymbol{q}}}\dot{\hat{\boldsymbol{q}}} + (\boldsymbol{\mu}_z)_{\boldsymbol{q}}\hat{\boldsymbol{q}} = 0 \\ \boldsymbol{\Phi}_q(\bar{\boldsymbol{q}})\hat{\boldsymbol{q}} = 0 \end{cases} \tag{41}$$

where

$$\begin{aligned} &\bar{\boldsymbol{M}} = \boldsymbol{M}(\bar{\boldsymbol{q}}), \qquad \bar{\boldsymbol{C}}_s = -\boldsymbol{P}_{\dot{\boldsymbol{q}}}, \qquad \bar{\boldsymbol{G}}_s = -\boldsymbol{Q}_{\dot{\boldsymbol{q}}} \\ &\bar{\boldsymbol{K}}_s = -\boldsymbol{P}_{\boldsymbol{q}} + [\boldsymbol{\Phi}_q^T\boldsymbol{\sigma}]_{\boldsymbol{q}} - \boldsymbol{Q}_{\boldsymbol{q}} \end{aligned} \tag{42}$$

The variable $\bar{\boldsymbol{M}}$ is computed according to Eq. (7), while $\bar{\boldsymbol{C}}_s$, $\bar{\boldsymbol{G}}_s$, and $\bar{\boldsymbol{K}}_s$ can be solved with an analytical or numerical Jacobian method [38].

With the presence of constraints, the generalized coordinate $\boldsymbol{q}$ is divided into two parts: independent generalized coordinate $\boldsymbol{q}^i$ and dependent generalized coordinate $\boldsymbol{q}^d$. Denoting $\boldsymbol{\Phi}_q^i$ and $\boldsymbol{\Phi}_q^d$ as the Jacobian matrices with respect to $\boldsymbol{q}^i$ and $\boldsymbol{q}^d$, the constraint equation in Eq. (41) can be written as

$$\boldsymbol{\Phi}_q^i(\bar{\boldsymbol{q}})\hat{\boldsymbol{q}}^i + \boldsymbol{\Phi}_q^d(\bar{\boldsymbol{q}})\hat{\boldsymbol{q}}^d = 0 \tag{43}$$

Using Eq. (43), $\hat{\boldsymbol{q}}$ can be expressed in terms of $\hat{\boldsymbol{q}}^i$ as

$$\hat{\boldsymbol{q}} = \boldsymbol{\Psi}\hat{\boldsymbol{q}}^i \tag{44}$$

where

$$\boldsymbol{\Psi} = \begin{bmatrix} \boldsymbol{I} \\ -(\boldsymbol{\Phi}_q^d)^{-1}\boldsymbol{\Phi}_q^i \end{bmatrix} \tag{45}$$

**Table 2 Model parameters of the whole aircraft model**

| Parameter | |
|---|---|
| Mass, kg | Fuselage: 40, wing segment: 10, tails: 10, fin: 10, rudder: 2, flap segment: 2, aileron segment: 2 |
| Rotational inertia $(J_x, J_y, J_z)$, kg · m$^2$ | Fuselage: (5.3, 100, 103.3), wing segment: (1.3, 25, 25.8), tails: (1.3, 25, 25.8), fin: (1.3, 25, 25,8), rudder: (0.26, 5, 5.2), flap segment: (0.26, 5, 5.2), aileron segment: (0.26, 5, 5.2) |
| Centroid coordinates $(x_C, y_C, z_C)$, m | Fuselage: (5.2, 0, 0), wing segment: (0, 0, 0), tails: (8.5, 1.6, 0), fin: (8.5, 0, −1.0), Rudder: (9.7, 0, −1.0), flap segment: (1, 1, 0), aileron segment: (1, 1, 0) |
| Young's modulus and Shear modulus, Pa | $5 \times 10^8$, $2 \times 10^8$ |
| Cross sectional area, m$^2$ | Wings: $2 \times 10^{-3}$, flaps and ailerons: $2 \times 10^{-3}$ |
| Inertia moment $(I_x, I_y, I_z)$, m$^4$ | Wings: $1 \times 10^{-3}$, $5 \times 10^{-4}$, $1 \times 10^{-2}$ flaps and ailerons: $1 \times 10^{-3}$, $5 \times 10^{-4}$, $1 \times 10^{-2}$ |
| Lift area, m$^2$ | Wings: 20 tails: 6.4, fin and rudder: 2.2 |
| Zero-lift angle of attack, rad | wings, tails, fin: −0.01205 control surface: 0.0 |
| Distance between the mass axis and the elastic axis, m | 0.1 |
| Distance of 1/4-chord to Elastic axis, m | 0.3 |

Substituting Eq. (44) into the first equation of Eq. (41) and premultiplying $\boldsymbol{\Psi}^T$, we can easily prove that

$$\boldsymbol{\Psi}^T \boldsymbol{\Phi}_q^T \hat{\boldsymbol{\sigma}} = 0 \tag{46}$$

The perturbation equation of the multibody system is obtained as

$$\bar{\boldsymbol{M}}^* \ddot{\hat{\boldsymbol{q}}}^i + (\bar{\boldsymbol{C}}_s^* + \bar{\boldsymbol{G}}_s^*)\dot{\hat{\boldsymbol{q}}}^i + \bar{\boldsymbol{K}}_s^* \hat{\boldsymbol{q}}^i = 0 \tag{47}$$

where

$$\bar{\boldsymbol{K}}_s^* = \boldsymbol{\Psi}^T \bar{\boldsymbol{K}}_s \boldsymbol{\Psi}, \qquad \bar{\boldsymbol{C}}_s^* = \boldsymbol{\Psi}^T \bar{\boldsymbol{C}}_s \boldsymbol{\Psi}, \qquad \bar{\boldsymbol{G}}_s^* = \boldsymbol{\Psi}^T \bar{\boldsymbol{G}}_s \boldsymbol{\Psi}$$
$$\bar{\boldsymbol{M}}^* = \boldsymbol{\Psi}^T \bar{\boldsymbol{M}} \boldsymbol{\Psi} \tag{48}$$

Through solving the characteristic equations of Eq. (47), the eigenvalues and eigenmodes of the system around the trim state can be solved, in which the stability of the system around this trim state can also be obtained.

## VIII. Examples and Discussions

As fundamental verification of the presented approach, the different modules (namely, 1-D structure, airfoil aerodynamics, and flight mechanics) have been verified separately with publicly available data [39]. In this section, the presented approach was applied to study the coupled behavior of flight dynamics and nonlinear aeroelasticity of a flexible aircraft. First, the trim and aeroelasticity of the wing was studied, then the trim condition of the flexible aircraft was obtained via dynamic relaxation under attitude and throttle controls. Next, the coupled flutter and flight dynamic behaviors of the flexible aircraft in level flight, as well as during the circling, loop, and dive–loop–climb maneuvers were studied. A flutter control law was designed to suppress limit cycle response and stabilize aircraft attitude in flight. This flutter control law was combined with the attitude and throttle control laws.

### A. Model Parameters of the Flexible Aircraft

The entire aircraft model was built using the presented approach. Table 2 lists all the model parameters of the entire aircraft model. The coordinate system $OXYZ$ that was fixed to the fuselage was built to

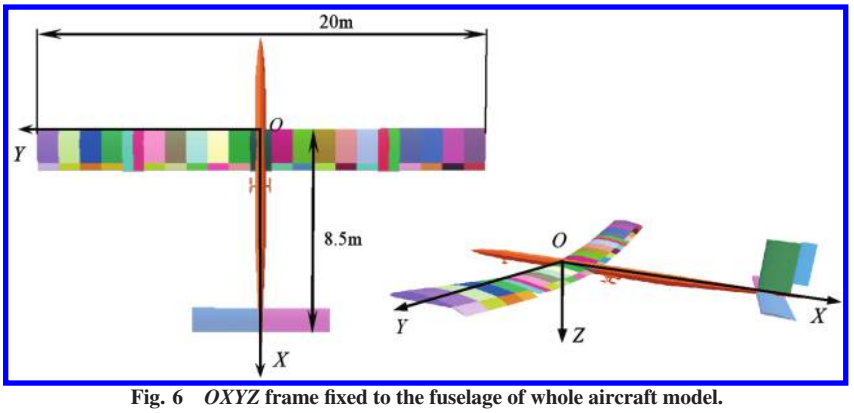


**Fig. 6 *OXYZ* frame fixed to the fuselage of whole aircraft model.**

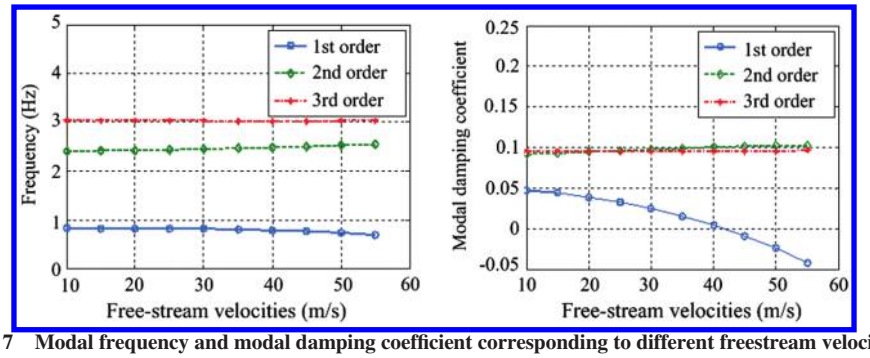


**Fig. 7 Modal frequency and modal damping coefficient corresponding to different freestream velocities.**

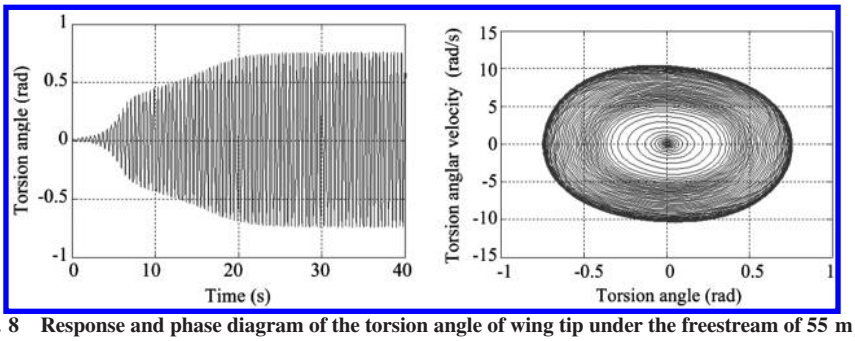


**Fig. 8 Response and phase diagram of the torsion angle of wing tip under the freestream of 55 m/s.**

determine the relative locations of the aircraft parts (Fig. 6). Its origin was located on the intersection point of the fuselage central axis and the wing mass axis. Its three coordinate axes point to the chordwise, spanwise, and downward directions, respectively. The wing was divided into 21 segments, the left and right ailerons were divided into four, and the dihedral and sweep angles were set as zero. The rigid model of the aircraft was obtained by increasing the Young's modulus and the shear modulus of the flexible wing by two orders of magnitude, simplifying the design of the flight control law.

### B. Aeroelastic Analysis of the Wing

The wing model was obtained by considering the one-sided wing of the entire aircraft model. Based on different freestream velocities, the response of the wing model was simulated to obtain the trim state, around which the perturbation equation was solved to determine critical flutter velocity.

In this example, the freestream velocity was set as 10 m/s initially and then increased by 5 m/s. The wing tip was excited by pulse, and its width was 0.01 s. Before the freestream speed reached 45 m/s, the trim states of the wing were obtained from the converged response. When the freestream speed exceeded 45 m/s, the diverged response from the trim state was simulated. The converged response was solved by numerically increasing the structural damping of the system to achieve the trim state. Then the structural damping of the system was restored, after which the perturbation equation around the trim state corresponding to every freestream speed was analyzed to obtain the modal frequency and damping of the system (Fig. 7). According to modal damping, the critical flutter speed was determined as 41.75 m/s, and the instability mode of the system was the first order.

When the freestream velocity exceeded that of critical flutter, the wing diverged from the trim state and converged to the limit cycle solution due to the structural nonlinearity and damping. Figure 8 shows the LCO response and phase diagram under the influence of the freestream of 55 m/s.

### C. Trimming of Flexible Aircraft in Level Flight

The trim condition of the flexible aircraft in level flight was obtained by the dynamic relaxation approach under attitude and throttle controls. The control law is listed in Table 3, where $k_p^{\mathrm{LE}}$, $k_p^{\mathrm{RE}}$, $k_p^{\mathrm{RA}}$, and $k_p^R$ are set as $-1$; $k_p^{\mathrm{LA}}$ is set as 1; $k_d^{\mathrm{LE}}$, $k_d^{\mathrm{RE}}$, $k_d^{\mathrm{RA}}$, and $k_d^R$ are set as $-0.25$; $k_p^p$ is set as 2520; and $k_d^p$ is set as 0. For the trimming of level flight at 55 m/s, the reference control signals are set as

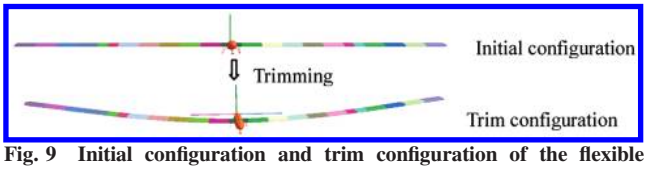


**Fig. 9 Initial configuration and trim configuration of the flexible aircraft in level flight.**

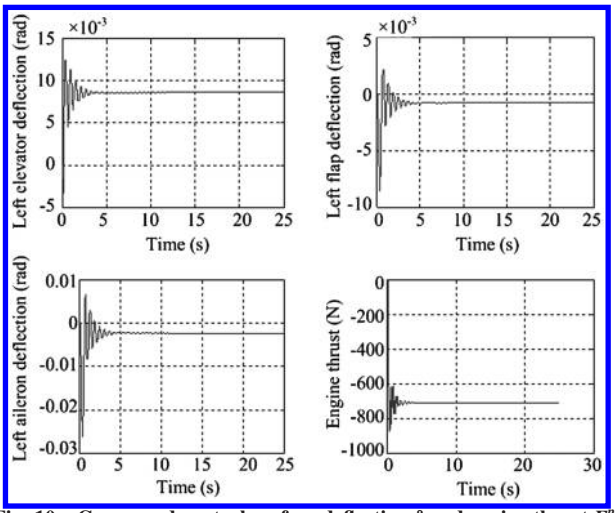


**Fig. 10 Converged control surface deflection $\delta$ and engine thrust $F^p$.**

$$\bar{\psi} = \dot{\bar{\psi}} = 0, \qquad \bar{\theta} = \dot{\bar{\theta}} = 0, \qquad \bar{\phi} = \dot{\bar{\phi}} = 0$$
$$\bar{v}^h = 55 \text{ m/s}, \qquad \bar{a}^h = 0 \tag{49}$$

By solving the governing system of Eq. (29) with the high structural damping under attitude and throttle controls, the flexible aircraft achieved the steady level flight state (Fig. 9). Meanwhile, the deflection $\delta$ of the control surfaces and the thrust $F^p$ of the engine converged to constants $\bar{\delta}$ and $\bar{F}^p$. These were taken as parameter settings for trim (Fig. 10).

### D. Aeroelastic Behavior of Aircraft in Level Flight

In this example, the aeroelastic behavior of the aircraft in level flight was studied at three velocities. The responses of torsion angle of the left wing are shown in Fig. 11. The critical flutter velocity of the entire aircraft can be determined as 44 m/s, which is greater than that

**Table 3 Flight control law**

| Input | Control law | Observed variables |
|---|---|---|
| $\delta_{\mathrm{LE}}^A$, $\delta_{\mathrm{RE}}^A$ | $\delta_{\mathrm{LE}}^A = k_p^{\mathrm{LE}}(\theta - \bar{\theta}) + k_d^{\mathrm{LE}}(\dot{\theta} - \dot{\bar{\theta}})$ and $\delta_{\mathrm{RE}}^A = k_p^{\mathrm{RE}}(\theta - \bar{\theta}) + k_d^{\mathrm{RE}}(\dot{\theta} - \dot{\bar{\theta}})$ | $\theta$ and $\dot{\theta}$ |
| $\delta_R^A$ | $\delta_R^A = k_p^R(\psi - \bar{\psi}) + k_d^R(\dot{\psi} - \dot{\bar{\psi}})$ | $\psi$ and $\dot{\psi}$ |
| $\delta_A^A$ | $\delta_{\mathrm{LA}}^A = k_p^{\mathrm{LA}}(\phi - \bar{\phi}) + k_d^{\mathrm{LA}}(\dot{\phi} - \dot{\bar{\phi}})$ and $\delta_{\mathrm{RA}}^A = k_p^{\mathrm{RA}}(\phi - \bar{\phi}) + k_d^{\mathrm{RA}}(\dot{\phi} - \dot{\bar{\phi}})$ | $\phi$ and $\dot{\phi}$ |
| $F^p$ | $F^p = k_p^p(v^{\mathrm{hf}} - \bar{v}^{\mathrm{hf}}) + k_d^p(a^{\mathrm{hf}} - \bar{a}^{\mathrm{hf}})$ | $v^{\mathrm{hf}}$ and $a^{\mathrm{hf}}$ |

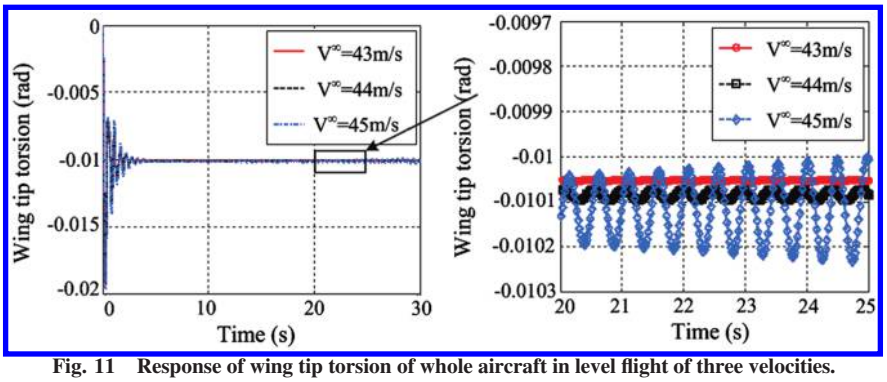


**Fig. 11 Response of wing tip torsion of whole aircraft in level flight of three velocities.**

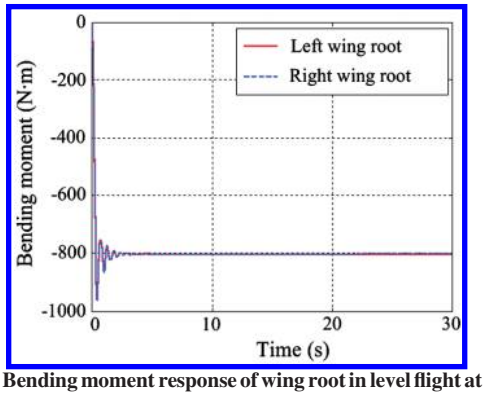


**Fig. 12 Bending moment response of wing root in level flight at 43 m/s.**

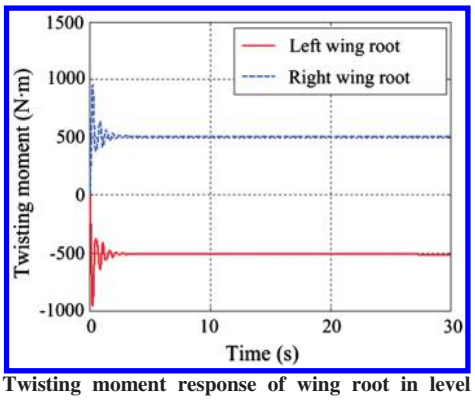


**Fig. 13 Twisting moment response of wing root in level flight at 43 m/s.**

of the wing model (41.75 m/s). The cause of the variation of critical flutter velocity is that the attitude control introduced the damping into the system, which increased the stability of the system brought about by the impact of structural nonlinearity.

The bending moment and twisting moment of the wing root is shown in Figs. 12 and 13.

**Fig. 14 Aircraft flutter mode at trimmed level flight.**

When the velocity of the flexible aircraft exceeded that of critical flutter, the wing of the aircraft also diverged from the trim state and converged to the limit cycle solution. Interestingly, the LCO response of the aircraft was dominated by the antisymmetric flutter mode coupled with fuselage roll (Fig. 14).

In this example, the airspeed was 55 m/s. Figure 15 shows the LCO responses of the torsion angle of the wing tips and the roll response of the fuselage.

A modal analysis was performed in order to obtain the rigid-body modes and wing elastic modes of the flexible aircraft. As shown in Figs. 16 and 17, the first elastic mode was a coupling one of the wing bend and the ups and downs of fuselage, and the second elastic mode was a coupling one of the wing bend, torsion, and fuselage roll. The second elastic mode dominated the response of the aircraft when the flutter occurred.

### E. Joint Control of Flutter and Attitude

Using the control law presented in Sec. VIII.C, the joint control of flutter and attitude was used to stabilize fuselage attitude and suppress LCO response. The accelerations of five measuring points were used as the observed variables of a feedback controller. The response of accelerometer 0, which was attached to the fuselage, was taken as the reference signal (Fig. 18). The uncontrolled and controlled responses of the wing tip are shown in Fig. 19. It indicates that the control law presented in Table 4 also controlled aircraft flutter effectively.

Interestingly, the suppression of flutter response induced the divergence of fuselage roll, as shown by the red line in Fig. 20. The fundamental reason for this phenomenon is given in the following analysis.

Figure 14 shows that the flutter response of the aircraft is dominated by the antisymmetric mode. The antisymmetric response is suppressed by control surface adjustment in accordance with the flutter control law, which produced the roll moment that induced fuselage roll divergence. Since the ailerons were applied to flutter control, they could not independently stabilize fuselage roll. Hence, it became necessary to seek the collaboration of other control surfaces. The two all-moving tails were used to provide auxiliary roll control by asynchronous rotation. Through the joint control, the LCO response was suppressed and fuselage roll was stabilized as shown by the blue line in Fig. 20.

### F. Trimming of the Aircraft in Circling Maneuver

The control law of the aircraft in a circling maneuver is discussed in this section. Through this law, the trim condition of the flexible aircraft was computed using the proposed dynamic relaxation approach. A circling maneuver can be obtained using ailerons and elevators. The fuselage was maintained at a constant roll angle by the ailerons to provide the centripetal force for circling. The pitch angle of the aircraft was adjusted by the all-moving tail to compensate for the lost lift force due to aircraft roll. Taking the altitude $h$, the pitch angle $\theta$, and its derivative $\dot{\theta}$ as the observed pitch control variables, the aircraft was maintained in a horizontal plane. The control law of the left and right tails is given by

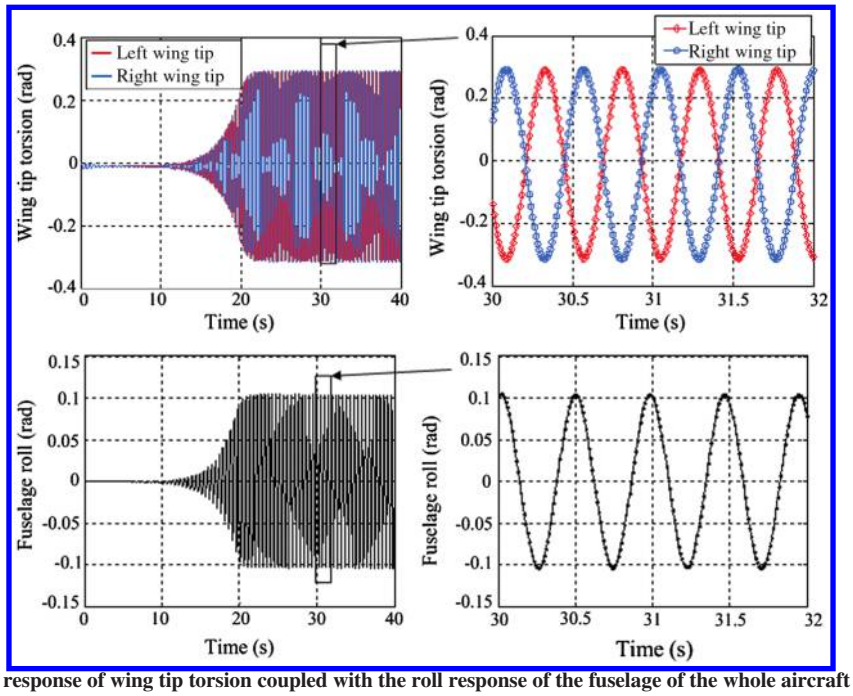


Fig. 15 LCO response of wing tip torsion coupled with the roll response of the fuselage of the whole aircraft in level flight.

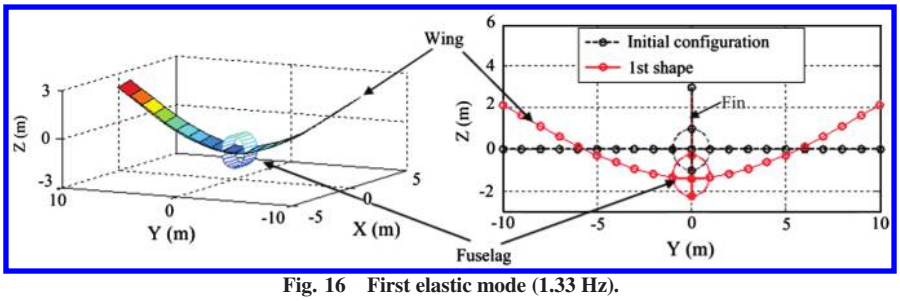


Fig. 16 First elastic mode (1.33 Hz).

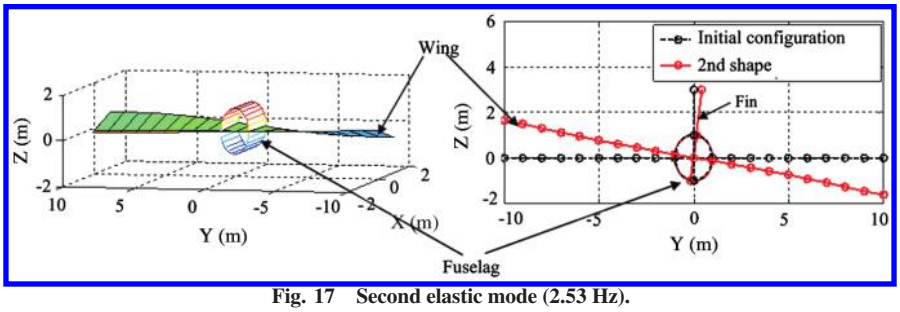


Fig. 17 Second elastic mode (2.53 Hz).

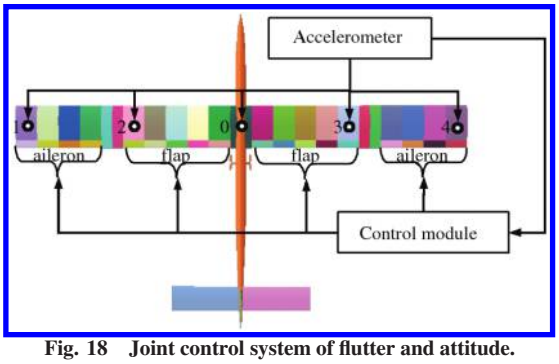


Fig. 18 Joint control system of flutter and attitude.

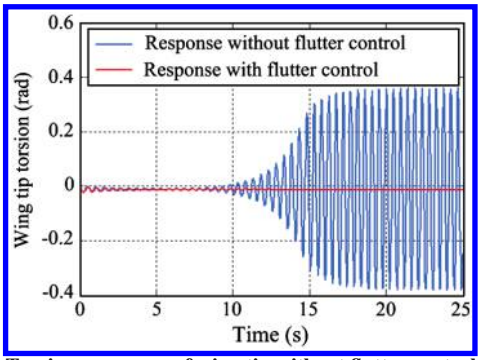


Fig. 19 Torsion responses of wing tip without flutter control and with flutter control.

**Table 4 Flutter control law**

| Sensor | Input | Feedback control transfer function | Observed variables |
|---|---|---|---|
| $a^{\text{pf}}$, $a_1^{\text{fw}}$, $a_2^{\text{fw}}$, $a_3^{\text{fw}}$, $a_4^{\text{fw}}$ | $\delta_{\text{LF}}^E$, $\delta_{\text{RF}}^E$, $\delta_{\text{LA}}^E$, $\delta_{\text{RA}}^E$ | $F(s) = -0.01\frac{3s+1}{s^2}$ | $a_2^{\text{fw}}$, $a_3^{\text{fw}}$, $a_1^{\text{fw}}$, $a_4^{\text{fw}}$ |

$$\delta_{\text{LE}}^A = \delta_{\text{RE}}^A = k_p^E(\theta - \bar{\theta}) + k_d^E(\dot{\theta} - \dot{\bar{\theta}}) + k_i^E(h - \bar{h}) \tag{50}$$

where $k_i^E$ is set as $\pi/180$, and the rudder control is removed. The control laws and control parameters of other control surfaces are the same as those shown in Table 3.

Using this attitude control law and the proposed trimming approach helped solve the trim condition for steady circling maneuver. The reference variables are set as

$$\bar{\psi} = \dot{\bar{\psi}} = 0, \qquad \bar{\phi} = \pi/4, \qquad \dot{\bar{\phi}} = 0$$
$$\bar{\theta} = (1/\cos\bar{\phi} - 1)\alpha^{L=0}, \qquad \dot{\bar{\theta}} = 0, \qquad \bar{v}^h = 55 \text{ m/s}$$
$$\bar{a}^h = 0, \qquad \bar{h} = \dot{\bar{h}} = 0 \tag{51}$$

The flexible aircraft achieved a steady circling maneuver by solving the governing system of Eq. (29) with high structural damping under attitude and throttle controls (Fig. 21). Meanwhile, the deflection $\delta$ of control surfaces and the thrust $F^p$ of the engine converged to constants $\bar{\delta}$ and $\bar{F}^p$; these were taken as the parameter settings for trim (see Fig. 22).

The circling loci of the rigid and flexible models of the aircraft under the same control law are, respectively, shown in Fig. 23. The turning radius of the rigid model is 590.7 m, and that of the flexible model is 595.9 m. Comparing the circling loci of the two models, the convergence speed of the flexible model is less than that of the rigid model.

### G. Aeroelastic Behavior of the Aircraft in Circling Maneuver

In this example, the aeroelastic behavior of the aircraft in a circling maneuver at two velocities was studied. The torsion angle responses of the left wing are shown in Fig. 24. The critical flutter velocity of the circling whole aircraft is 27.2 m/s, which is much less than that of the wing model (41.75 m/s) and that of the aircraft in level flight (44 m/s). This result shows that it is dangerous to substitute the aeroelasticity of the circling whole aircraft with that of the wing model. For the circling aircraft, due to the effects of Coriolis force and centrifugal force, the aerodynamic forces acting on the two wings were asymmetric, which resulted in an easily excited antisymmetric mode.

When the velocity of the flexible aircraft exceeded that of critical flutter, the wing of the aircraft also diverged from the trim state. Similar to the response of the aircraft in level flight, the circling maneuver was dominated by the antisymmetric flutter mode coupled with fuselage roll. Figure 25 shows the flutter responses of the torsion angles of the left and right wing tips.

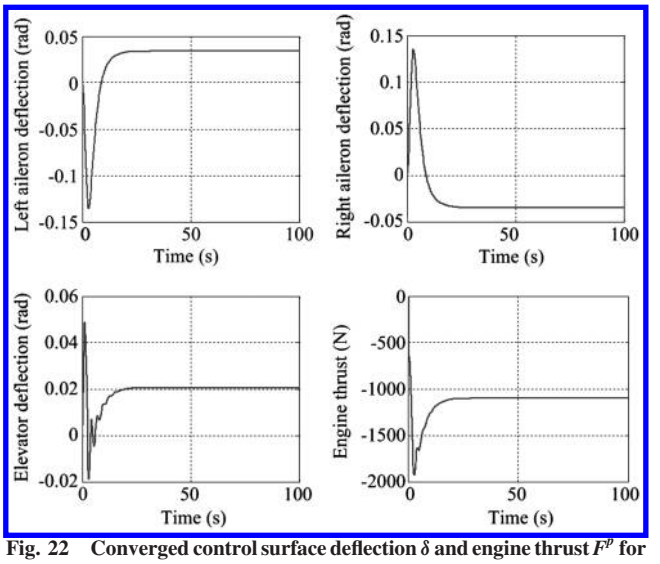


**Fig. 22 Converged control surface deflection $\delta$ and engine thrust $F^p$ for steady circling trim.**

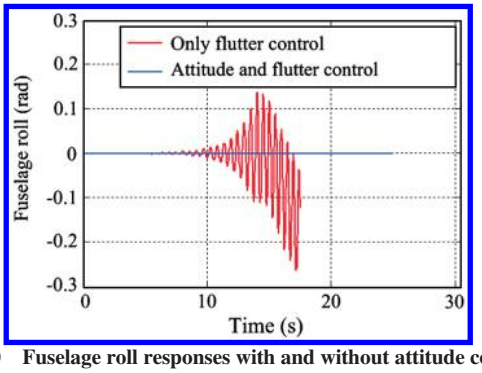


**Fig. 20 Fuselage roll responses with and without attitude control.**

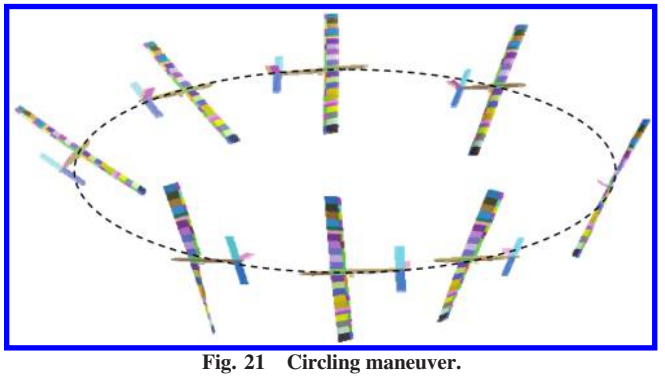

**Fig. 21 Circling maneuver.**

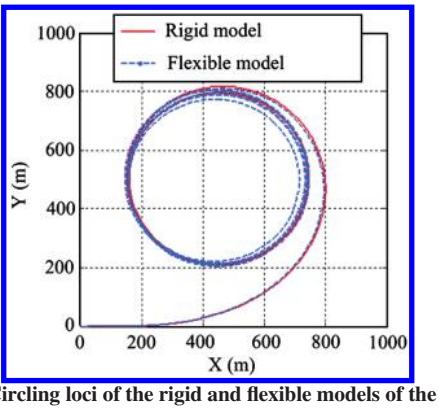


**Fig. 23 Circling loci of the rigid and flexible models of the aircraft.**

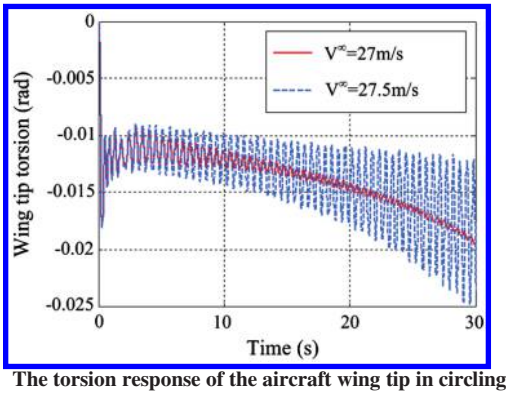


**Fig. 24 The torsion response of the aircraft wing tip in circling at two velocities.**

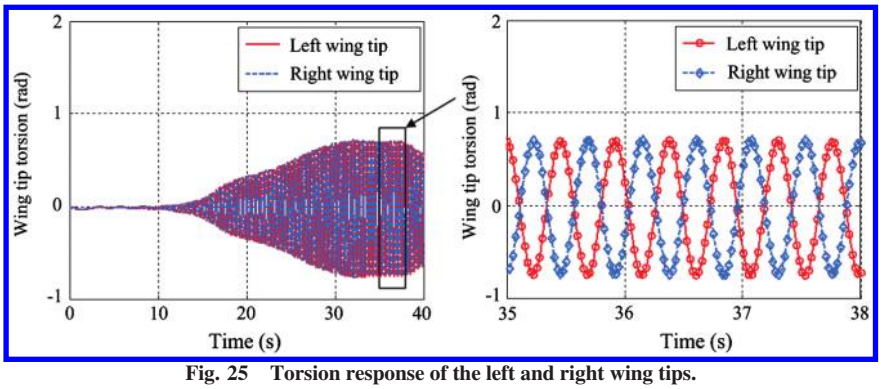


Fig. 25 Torsion response of the left and right wing tips.

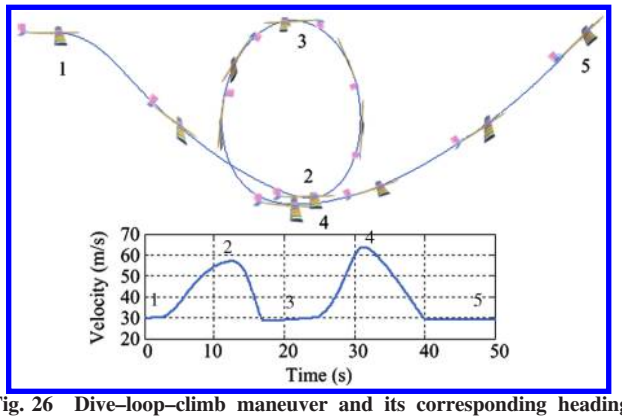


Fig. 26 Dive–loop–climb maneuver and its corresponding heading velocity.

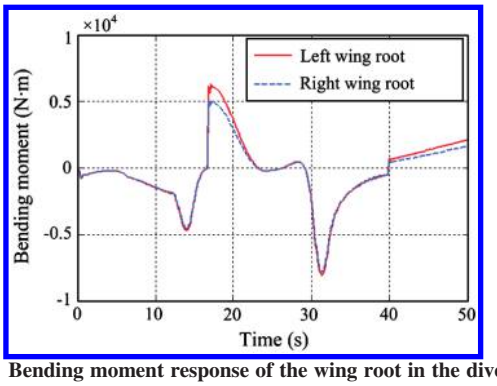


Fig. 28 Bending moment response of the wing root in the dive–loop–climb maneuver.

The difference from level flight lay in the fact that the diverged response in a circling maneuver never converged to the stable limit cycle solution because the steady circling was disturbed by flutter. When the wing fluttered, the varying aerodynamic force was exerted upon the fuselage through the wing root, inducing attitude divergence.

### H. Flight Control and Aeroelasticity in the Dive–Loop–Climb Maneuvers

Dive, loop, and climb are three typical longitudinal maneuvers that are usually combined. The control law of the aircraft in the combinatorial maneuver consisting of dive, loop, and climb is discussed in this section, and the aeroelastic response of the flexible aircraft in this maneuver is solved. This combinatorial maneuver can be obtained by the control of the elevator or all-moving tail, where the angular velocity of the left and right tails is set as

$$\dot{\delta}^A_{\mathrm{LE}} = \dot{\delta}^A_{\mathrm{RE}} = \begin{cases} (\pi/60)\sin(\pi t/6) & t \le 6 \\ 0 & 6 < t \le 12 \\ -\pi(t-12)/96 & 12 < t \le 14 \\ -\pi/48 & 14 < t \le 30 \\ -\pi/48 + \pi(t-30)/96 & 30 < t \le 32 \\ 0 & t > 32 \end{cases} \quad (52)$$

The control laws of other control surfaces were the same as that for level flight, for which the reference variables are set as

$$\bar{\psi} = \dot{\bar{\psi}} = 0, \qquad \bar{\phi} = \dot{\bar{\phi}} = 0, \qquad \bar{v}^{\mathrm{hf}} = 30\ \mathrm{m/s}, \qquad \bar{a}^{\mathrm{hf}} = 0 \quad (53)$$

The combinatorial maneuver was achieved under these control inputs (Fig. 26), in which several numbers and markers provided the relationship between the location and heading velocity of the aircraft. The initial velocity of the aircraft was set as 30 m/s. Because of the dive and loop acceleration, the aircraft speed exceeded the critical flutter velocity, and the wing of the aircraft also diverged from the trim state.

Similar to the response of the aircraft in level flight and in the circling maneuver, the aeroelastic response of the aircraft in the combinatorial maneuver was dominated by the antisymmetric flutter mode coupled with fuselage roll. Figure 27 shows the aeroelastic responses of the torsion angle of the left and right wing tips. When the aircraft entered the climb stage, aircraft speed was reduced rapidly before finally returning to a steady state.

The bending and twisting moments of the wing root are shown in Figs. 28 and 29. As can be seen, the structural internal force changes rapidly with the occurrence of flutter, for which further flutter suppression are required before this maneuver.

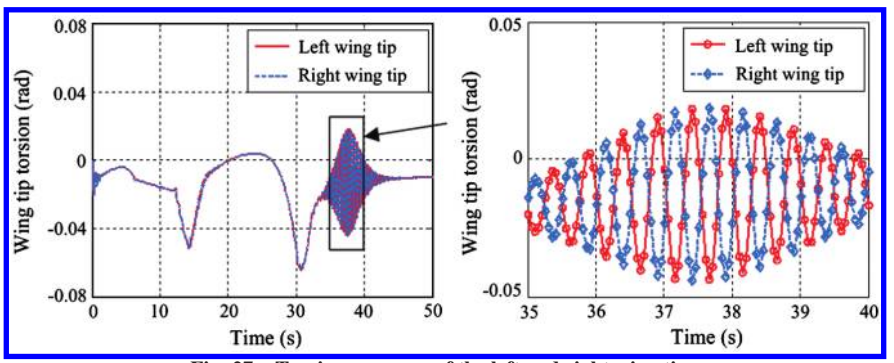


Fig. 27 Torsion response of the left and right wing tips.

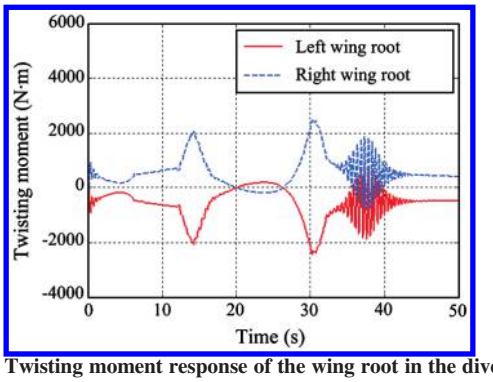


**Fig. 29 Twisting moment response of the wing root in the dive–loop–climb maneuver.**

## IX. Conclusions

With the development of multibody dynamics, studying the coupled behavior of flight dynamics and aeroelasticity of the flexible aircraft in level flight and maneuvers such as circling, loop, and dive–loop–climb has become possible. To achieve this goal, the integrated approach of flight dynamics and nonlinear aeroelasticity was presented in this paper. The multibody dynamic equation was a DAE, in which the constrained system containing rigid and flexible components was conveniently modeled. Furthermore, the governing equations of the flexible aircraft, consisting of the multibody dynamic equations, ONERA aerodynamic equations and control state equations, were established; in turn, these made it feasible to integrally study flight dynamics, aeroelasticity, and the flexible aircraft. In this paper, the methods for trimming and stability analyses based on multibody dynamics were also provided. These methods were used to determine trim condition by solving the governing equations with trim flight parameters as the control target in the time domain: i.e., dynamic relaxation method. Then the flutter critical velocity and instability mode of the system was determined by the perturbation equations around the trim state.

Through simulation of the flexible aircraft in level flight and different maneuvers, several interesting aspects of the flexible aircraft flutter were revealed. First, the antisymmetric flutter mode involving the fuselage roll was found. The simulation showed that the suppression of flutter response induced the divergence of fuselage roll and it is necessary to include the attitude control in the suppression of flutter. This study likewise found that the critical flutter velocities of flexible aircraft varied with the different types of maneuvers.

The approach presented in this paper can be used to study the coupling dynamic behavior of a maneuvering flexible aircraft as well as model the constrained system that undergoes large displacements and rotations with mechanisms such as joints. As a time-domain approach, this approach is expected to be used in conceptual aircraft design. However, as for the determination of the flutter boundary, the classical frequency-domain aeroelastic approaches are more convenient.

For future studies, the flutter control for the circling and dive–loop–climb maneuvers is expected to be studied. The absolute nodal coordinate formulation beam is a potential approach for the nonlinear structures with large deformations and large rotations. In terms of the absolute nodal coordinate formulation shell element and the unsteady vortex-lattice aerodynamic model, this approach is expected to be generalized to the wing characterized by a complex geometry configuration.

## References

[1] Patil, M. J., Hodges, D. H., and Cesnik, C. E. S., "Nonlinear Aeroelasticity and Flight Dynamics of High-Altitude Long-Endurance Aircraft," *Journal of Aircraft*, Vol. 38, No. 1, 2001, pp. 88–94. doi:10.2514/2.2738

[2] Cesnik, C. E. S., Senatore, P. J., Su, W., and Atkins, E. M., "X-HALE: A Very Flexible UAV for Nonlinear Aeroelastic Tests," AIAA Paper 2010-2715, April 2010.

[3] Nguyen, N., "Integrated Flight Dynamic Modeling of Flexible Aircraft with Inertial Force-Propulsion-Aeroelastic Coupling," AIAA Paper 2008-194, Jan. 2008.

[4] Bisplinghoff, R. L., Ashley, H., and Halfman, R. L., *Aeroelasticity*, Addison-Wesley, Cambridge, MA, 1955.

[5] Fung, Y. C., *An Introduction to the Theory of Aeroelasticity*, Wiley, New York, 1955.

[6] Dowell, E. H., *A Modern Course in Aeroelasticity*, Sijthoff & Noordhoff, Alphen aan den Rijn, The Netherlands, 1978.

[7] Dowell, E., Edwards, J., and Strganac, T., "Nonlinear Aeroelasticity," *Journal of Aircraft*, Vol. 40, No. 5, 2003, pp. 857–874. doi:10.2514/2.6876

[8] Dowell, E. H., and Tang, D., "Nonlinear Aeroelasticity and Unsteady Aerodynamics," *AIAA Journal*, Vol. 40, No. 9, 2002, pp. 1697–1707. doi:10.2514/2.1853

[9] Schnittger, J. R., "Single Degree of Freedom Flutter of Compressor Blades in Separated Flow," *Journal of the Aeronautical Sciences*, Vol. 21, No. 1, 1954, pp. 27–36.

[10] Dowell, E. H., "Nonlinear Aeroelasticity," AIAA Paper 1990-1031, April 1990.

[11] Patil, M. J., and Hodges, D. H., "Flight Dynamics of Highly Flexible Flying Wings," *Journal of Aircraft*, Vol. 43, No. 6, 2006, pp. 1790–1799. doi:10.2514/1.17640

[12] Chang, C. S., Hodges, D. H., and Patil, M. J., "Flight Dynamics of Highly Flexible Aircraft," *Journal of Aircraft*, Vol. 45, No. 2, 2008, pp. 538–545. doi:10.2514/1.30890

[13] Shearer, C., and Cesnik, C., "Nonlinear Flight Dynamics of Very Flexible Aircraft," *Journal of Aircraft*, Vol. 44, No. 5, 2007, pp. 1528–1545. doi:10.2514/1.27606

[14] Meirovitch, L., and Tuzcu, I., "Unified Theory for the Dynamics and Control of Maneuvering Flexible Aircraft," *AIAA Journal*, Vol. 42, No. 4, 2004, pp. 714–727. doi:10.2514/1.1489

[15] Shabana, A. A., "Flexible Multibody Dynamics: Review of Past and Recent Developments," *Multibody System Dynamics*, Vol. 1, No. 2, 1997, pp. 189–222. doi:10.1023/A:1009773505418

[16] Haug, E. J., *Computer Aided Kinematics and Dynamics of Mechanical Systems, Volume 1: Basic Methods*, Allyn and Bacon, Boston, 1989.

[17] Huston, R. L., *Multibody Dynamics*, Butterworths, Boston, 1990.

[18] Møller, H., Lund, E., Ambrosio, J. A. C., and Goncalves, J., "Simulation of Fluid Loaded Flexible Multibody Systems," *Multibody System Dynamics*, Vol. 13, No. 1, 2005, pp. 113–128. doi:10.1007/s11044-005-2531-x

[19] Samin, J. C., Brüls, O., Collard, J. F., Sass, L., and Fisette, P., "Multiphysics Modeling and Optimization of Mechatronic Multibody Systems," *Multibody System Dynamics*, Vol. 18, No. 3, 2007, pp. 345–373. doi:10.1007/s11044-007-9076-0

[20] Bauchau, O. A., Bottasso, C. L., and Nikishkov, Y. G., "Modeling Rotorcraft Dynamics with Finite Element Multibody Procedures," *Mathematical and Computer Modelling*, Vol. 33, No. 10–11, 2001, pp. 1113–1137. doi:10.1016/S0895-7177(00)00303-4

[21] Das, M., Barut, A., Madenci, E., and Straub, F., "Nonlinear Flexible Multibody Dynamic Analysis of Rotor Blades with a Trailing Edge Flap," AIAA Paper 2006-1862, May 2006.

[22] Das, M., Barut, A., Madenci, E., and Straub, F., "Aeroelastic Analysis of Rotor Blades Using Three Dimensional Flexible Multibody Dynamic Analysis," AIAA Paper 2007-2295, April 2007.

[23] Scarlett, J. N., Canfield, R. A., and Sanders, B., "Multibody Dynamic Aeroelastic Simulation of a Folding Wing Aircraft," AIAA Paper 2006-2135, May 2006.

[24] Nikravesh, P. E., Wehage, R. A., and Kwon, O. K., "Euler Parameters in Computational Dynamics and Kinematics. Parts I and II," *Journal of Mechanisms, Transmissions, and Automation in Design*, Vol. 107, No. 3, 1985, pp. 358–369. doi:10.1115/1.3260722

[25] Fowles, G. R., *Analytical Mechanics*, Holt Rienhart and Winston, New York, 1977.

[26] Connelly, J. D., and Huston, R. L., "The Dynamics of Flexible Multibody Systems-A Finite Segment Approach. I: Theoretical Aspects," *Computers and Structures*, Vol. 50, No. 2, 1994, pp. 255–258. doi:10.1016/0045-7949(94)90300-X

[27] Cheng, Y., Dai, S. L., and Ren, G. X., "A Hybrid Finite Segment/Finite Element Modelling and Experiment on a Flexible Deployment System," *Journal of Sound and Vibration*, Vol. 258, No. 5, 2002, pp. 931–949. doi:10.1006/jsvi.2002.5135

[28] Rodden, W. P., "Aerodynamic Influence Coefficients from Strip Theory," *Journal of the Aeronautical Sciences*, Vol. 26, 1959, pp. 833–834.

[29] Friedmann, P. P., and Hodges, D. H., "Rotary Wing Aeroelasticity—A Historical Perspective," *Journal of Aircraft*, Vol. 40, No. 6, 2003, pp. 1019–1046. doi:10.2514/2.7216

[30] Kim, T., and Dugundji, J., "Nonlinear Large Amplitude Aeroelastic Behavior of Composite Rotor Blades," *AIAA Journal*, Vol. 31, No. 8, 1993, pp. 1489–1497. doi:10.2514/3.49082

[31] Dunn, P. E., and Dugundji, J., "Nonlinear Stall Flutter and Divergence Analysis of Cantilevered Graphite/Epoxy Wings," *AIAA Journal*, Vol. 30, No. 1, 1992, pp. 153–162. doi:10.2514/3.10895

[32] Bernard, E., and Reid, L. D., *Dynamics of Flight: Stability and Control*, Wiley, New York, 1996.

[33] William, L. B., *Modern Control Theory*, Prentice Hall, Englewood Cliffs, NJ, 1991.

[34] Hairer, E., Norsett, S. P., and Wanner, G., *Solving Ordinary Differential Equations*, Springer–Verlag, Berlin, 1987.

[35] Chudoba, B., and Cook, M. V., "Trim Equations of Motion for Aircraft Design: Steady State Straight-Line Flight," AIAA Paper 2003-5691, Aug. 2003.

[36] Chudoba, B., and Cook, M. V., "Trim Equations of Motion for Aircraft Design: Turning Flight, Pull-Up and Push-Over," AIAA Paper 2003-5693, Aug. 2003.

[37] Chudoba, B., and Cook, M. V., "Trim Equations of Motion for Aircraft Design: Rolling Performance and Take-Off Rotation," AIAA Paper 2003-5695, Aug. 2003.

[38] Shampine, L. F., and Reichelt, M. W., "The MATLAB ODE Suite," *SIAM Journal on Scientific Computing*, Vol. 18, No. 1, 1997, pp. 1–22. doi:10.1137/S1064827594276424

[39] Zhao, Z. J., "Multibody Dynamic Approach for Coupling Analysis of Nonlinear Aeroelasticity and Flight Dynamics," Ph.D. Dissertation, Tsinghua Univ., Beijing, PRC, 2009.

C. Cesnik
*Associate Editor*

**This article has been cited by:**


1. Chao AN, Chao YANG, Changchuan XIE, Lan YANG. 2020. Flutter and gust response analysis of a wing model including geometric nonlinearities based on a modified structural ROM. *Chinese Journal of Aeronautics* **33**:1, 48-63. [Crossref]
2. Han Wu, Zhengping Wang, Zhou Zhou, Rui Wang. 2019. Modeling and Simulation for Multi-Rotor Fixed-Wing UAV Based on Multibody Dynamics. *Xibei Gongye Daxue Xuebao/Journal of Northwestern Polytechnical University* **37**:5, 928-934. [Crossref]
3. Han Wu, Zhengping Wang, Zhou Zhou, Jieyu Jia, Rui Wang. Modeling of Small UAV Parachute Recovery System Based on Lagrangian Method 1127-1132. [Crossref]
4. Heming Zheng, Guang Zhai. 2019. Attitude dynamics of coupled spacecraft undergoing fuel transfer. *Multibody System Dynamics* **46**:4, 355-379. [Crossref]
5. Chao An, Chao Yang, Changchuan Xie, Yang Meng. 2019. Gust Load Alleviation including Geometric Nonlinearities Based on Dynamic Linearization of Structural ROM. *International Journal of Aerospace Engineering* **2019**, 1-20. [Crossref]
6. Amir Hossein Modaress-Aval, Firooz Bakhtiari-Nejad, Earl H. Dowell, David A. Peters, Hossein Shahverdi. 2019. A comparative study of nonlinear aeroelastic models for high aspect ratio wings. *Journal of Fluids and Structures* **85**, 249-274. [Crossref]
7. Qingjun Li, Zichen Deng, Kai Zhang, He Huang. 2018. Unified Modeling Method for Large Space Structures Using Absolute Nodal Coordinate. *AIAA Journal* **56**:10, 4146-4157. [Abstract] [Full Text] [PDF] [PDF Plus]
8. A. Castrichini, J. E. Cooper, T. Benoit, Y. Lemmens. 2018. Gust and Ground Loads Integration for Aircraft Landing Loads Prediction. *Journal of Aircraft* **55**:1, 184-194. [Abstract] [Full Text] [PDF] [PDF Plus]
9. S. Preidikman, B. A. Roccia, M. L. Verstraete, L. R. Ceballos, B. Balachandran. A Computational Aeroelastic Framework for Studying Non-conventional Aeronautical Systems 325-334. [Crossref]
10. Michele Castellani, Jonathan E. Cooper, Yves Lemmens. 2017. Nonlinear Static Aeroelasticity of High-Aspect-Ratio-Wing Aircraft by Finite Element and Multibody Methods. *Journal of Aircraft* **54**:2, 548-560. [Abstract] [Full Text] [PDF] [PDF Plus]
11. Frederico Afonso, José Vale, Éder Oliveira, Fernando Lau, Afzal Suleman. 2017. A review on non-linear aeroelasticity of high aspect-ratio wings. *Progress in Aerospace Sciences* **89**, 40-57. [Crossref]
12. Andrea Castrichini, Jonathan E. Cooper, Tuur Benoit, Yves Lemmens. Gust and Ground Loads Integration for Aircraft Landing Loads Prediction . [Citation] [PDF] [PDF Plus]
13. Yinan Wang, Andrew Wynn, Rafael Palacios. 2016. Nonlinear Modal Aeroservoelastic Analysis Framework for Flexible Aircraft. *AIAA Journal* **54**:10, 3075-3090. [Abstract] [Full Text] [PDF] [PDF Plus]
14. Wei Wang, Xiaoping Zhu, Zhou Zhou, Jingbo Duan. 2016. A method for nonlinear aeroelasticity trim and stability analysis of very flexible aircraft based on co-rotational theory. *Journal of Fluids and Structures* **62**, 209-229. [Crossref]
15. Michele Castellani, Jonathan E. Cooper, Yves Lemmens. Nonlinear Static Aeroelasticity of High Aspect Ratio Wing Aircraft by FEM and Multibody methods . [Citation] [PDF] [PDF Plus]
16. Chris Howcroft, Dario Calderon, Luke Lambert, Michele Castellani, Jonathan E. Cooper, Mark H. Lowenberg, Simon Neild. Aeroelastic Modelling of Highly Flexible Wings . [Citation] [PDF] [PDF Plus]
17. Michele Castellani, Jonathan E. Cooper, Yves Lemmens. 2016. Flight Loads Prediction of High Aspect Ratio Wing Aircraft Using Multibody Dynamics. *International Journal of Aerospace Engineering* **2016**, 1-13. [Crossref]
18. Jintao Yin, Juanmian Lei, Xiaosheng Wu, Tianyu Lu. 2015. Effect of elastic deformation on the aerodynamic characteristics of a high-speed spinning projectile. *Aerospace Science and Technology* **45**, 254-264. [Crossref]
19. Ilhan Tuzcu, Nhan Nguyen. 2015. Flutter of Maneuvering Aircraft. *Journal of Aerospace Engineering* **28**:4, 04014094. [Crossref]
20. Justin M. Selfridge, Gang Tao. Centrifugally Stiffened Rotor: A Complete Derivation of the Plant Model with Nonlinear Dynamics . [Citation] [PDF] [PDF Plus]
21. Jinwu Xiang, Yongju Yan, Daochun Li. 2014. Recent advance in nonlinear aeroelastic analysis and control of the aircraft. *Chinese Journal of Aeronautics* **27**:1, 12-22. [Crossref]
22. H. Sadat-Hoseini, S. A. Fazelzadeh, A. Rasti, P. Marzocca. 2013. Final Approach and Flare Control of a Flexible Aircraft in Crosswind Landings. *Journal of Guidance, Control, and Dynamics* **36**:4, 946-957. [Abstract] [Full Text] [PDF] [PDF Plus]

23. Y. Yu, Q. Yang, X. Wang. 2013. Finite element analysis of fluid–structure interaction for the design of MAV aerodynamic shape. *Computers & Fluids* **76**, 50-57. [Crossref]
24. A. RASTI, S. A. FAZELZADEH. 2012. MULTIBODY DYNAMIC MODELING AND FLUTTER ANALYSIS OF A FLEXIBLE SLENDER VEHICLE. *International Journal of Structural Stability and Dynamics* **12**:06, 1250049. [Crossref]
25. Joseba Murua, Rafael Palacios, J. Michael R. Graham. 2012. Applications of the unsteady vortex-lattice method in aircraft aeroelasticity and flight dynamics. *Progress in Aerospace Sciences* **55**, 46-72. [Crossref]
26. Henrik Hesse, Joseba Murua, Rafael Palacios. Consistent Structural Linearization in Flexible Aircraft Dynamics with Large Rigid-Body Motion . [Citation] [PDF] [PDF Plus]
27. Joseba Murua, Rafael Palacios, J.m.r. Graham. Open-Loop Stability and Closed-Loop Gust Alleviation on Flexible Aircraft Including Wake Modeling . [Citation] [PDF] [PDF Plus]